Groundwater flow paths using combined self-potential, electrical resistivity, and induced polarization signals

André Revil, A Ghorbani, X Zhao, A Mouyeaux, L Barrère, J Richard, L Peyras, P Vaudelet

Geophysical Journal International

Geophys. J. Int. (2024) **239,** 798–820
Advance Access publication 2024 August 20
GJI Applied and Marine Geophysics

https://doi.org/10.1093/gji/ggae291

Groundwater flow paths using combined self-potential, electrical resistivity, and induced polarization signals

A. Revil,[1] A. Ghorbani,[2] X. Zhao,[1,3] A. Mouyeaux,[4] L. Barrère,[5] J. Richard,[2] L. Peyras[4] and P. Vaudelet[2]

[1] *Université Grenoble Alpes, Université Savoie Mont-Blanc, CNRS, UMR CNRS* 5204, *EDYTEM,* F-73370 *Le Bourget du Lac, France. E-mail: andre.revil@univ-smb.fr*
[2] *Naga Geophysics, Technolac,* F-73370 *Le Bourget du Lac, France*
[3] *College of Earth Science and Engineering, Hohai University, Nanjing* 211100, *China*
[4] *INRAE, UMR RECOVER, Aix-Marseille Université, F-13080, Aix-en-Provence, France*
[5] *Voies Navigables de France, 175, rue Ludovic Boutleux, F-62408 Béthune, France*

Accepted 2024 August 19. Received 2024 August 16; in original form 2024 February 12

SUMMARY

The dam of Lampy (Black Mountain, Aude, France) is considered as one of the oldest dams in France. A geophysical survey is performed to better understand the pattern of groundwater flow downstream of this dam in the granitic substratum. Induced polarization is first used to image both electrical conductivity and normalized chargeability. Eight core samples of granite from this site are measured and analysed in the laboratory. Their electrical conductivity and normalized chargeability are expressed as a function of the porosity and cation exchange capacity (CEC). The field data and the petrophysical results are used to image the water content, the CEC and the permeability distribution of the substratum. Then, self-potential is used as a complementary passive geophysical technique, which, in absence of metallic bodies, is directly sensitive to groundwater flow through the so-called streaming potential effect. Indeed, the excess of electrical charges in the vicinity of the solid grains, in the so-called double layer, is dragged by the ground water flow generating in turn an electrical (streaming) current and therefore an electrical field. A map of the resulting self-potential signals is done over the area covered by the induced polarization profiles. This map shows a large positive anomaly with an amplitude of ∼80 mV possibly associated with upwelling groundwater in an area where the soil is water-saturated. A groundwater flow simulation is performed to model this anomaly. This is done in two steps. A preliminary groundwater flow model is built using the permeability and water content distributions obtained from the induced polarization data. Then, this groundwater flow model is updated using the information contained in the self-potential data including the electrical conductivity distribution obtained through resistivity tomography. The algorithm for the inversion of the self-potential data is validated through a 2-D numerical test. This analysis yields a groundwater flow model with the flow being focused through a high permeability zone. This study shows how three geoelectrical methods (self-potential, induced polarization and electrical resistivity) can be efficiently combined to image groundwater flow in the vicinity of a dam.

Key words: Electrical properties; Permeability and porosity; Electrical resistivity tomography (ERT); Induced polarization; Hydrogeophysics.

1. INTRODUCTION

Geoelectrical methods are considered to be powerful and non-intrusive methods to image subsurface properties in a variety of environments (Karaoulis *et al.* 2011; Revil *et al.* 2012; Binley *et al.* 2015). This is especially true in the realm of hydrogeology, for instance in order to characterize groundwater flow and leaks potentially present in dams and embankments (e.g. Panthulu *et al.* 2001; Ling *et al.* 2019; Soueid Ahmed *et al.* 2019, 2020a, b).

The self-potential method (Rozycki *et al.* 2006; Soueid Ahmed *et al.* 2019; Xie *et al.* 2021), the electrical conductivity/resistivity method (Fransisco *et al.* 2018; Himi *et al.* 2018) and the induced

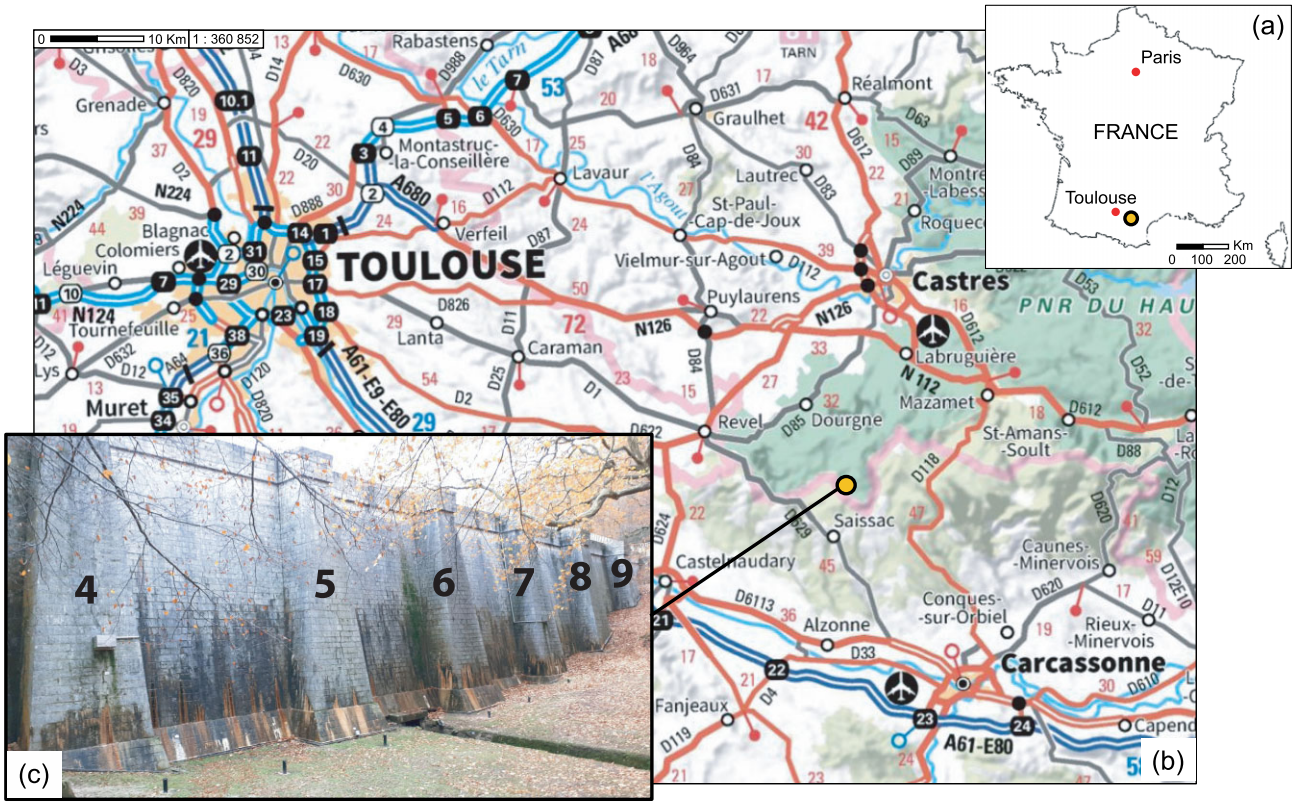

Figure 1. Lampy dam in France. (a) Localization of the dam in the South of France (the position of the dam is shown by the open circle). (b) The dam is located in the Black Mountains between the cities of Toulouse and Carcassonne (position of the dam: open circle). (c) Picture of the dam built in 1782. The dam is made of granite blocks cemented with lime. The picture shows 6 of the 10 buttresses (labelled 1–10 through the paper). At the feet of buttress 8, we observe the presence of a small spring.

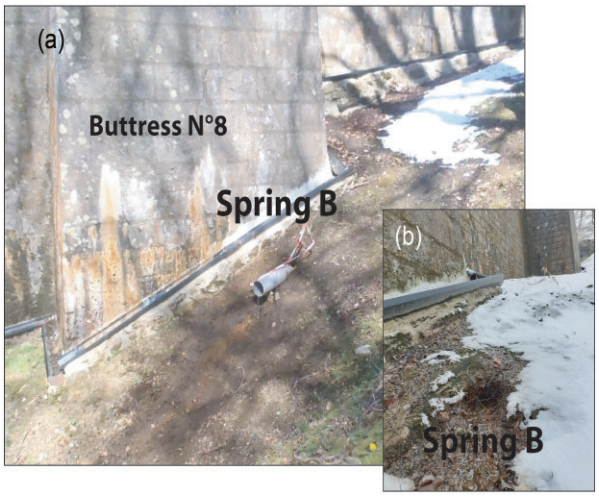

Figure 2. Position of the Spring B at the toe of buttress 8. (a) Picture showing the spring channelled here at its outlet through a pipe to monitor and quantify the outflow rate. (b) Picture showing the spring in winter. This observation raises the question to know if this spring can be considered as a leak or a short-path ground water flow associated with one of the water channel located a bit above the spring.

polarization method (Abdulsamad *et al.* 2019) have independently played a role in localizing leakages and flow patterns in dams and embankments.

Induced polarization is an active galvanometric (geoelectrical) method used to image the subsurface normalized chargeability (in addition to electrical conductivity, see Titov *et al.* 2002; Kemna *et al.* 2012, and references therein). The electrical conductivity describes the ability of a rock/sediment to let the current flow through when submitted to an imposed electrical field. The normalized chargeability describes the ability of the material to store electrical charges and to reversibly 'discharge' when the applied electrical field is removed (e.g. Shuey & Johnson 1973; Soueid Ahmed *et al.* 2018). Developed initially by Schlumberger (1920) for the exploration of ores, this prospecting method is now broadly used in environmental geophysics (e.g. Börner *et al.* 1993; Johnson *et al.* 2010; Binley *et al.* 2015). Its underlying physics can be understood thanks to pore scale models (Rosen *et al.* 1993; Revil 2013a, b).

The electrical conductivity and normalized chargeability are influenced by the electrical double layer coating the surface of the grains and formed by the Stern and Gouy–Chapman diffuse layers at the nanoscale (e.g. Waxman & Smits 1968; Vinegar & Waxman 1984; Hao *et al.* 2016; Niu *et al.* 2016). The Stern is associated with weakly sorbed counterions onto the surface of the grains

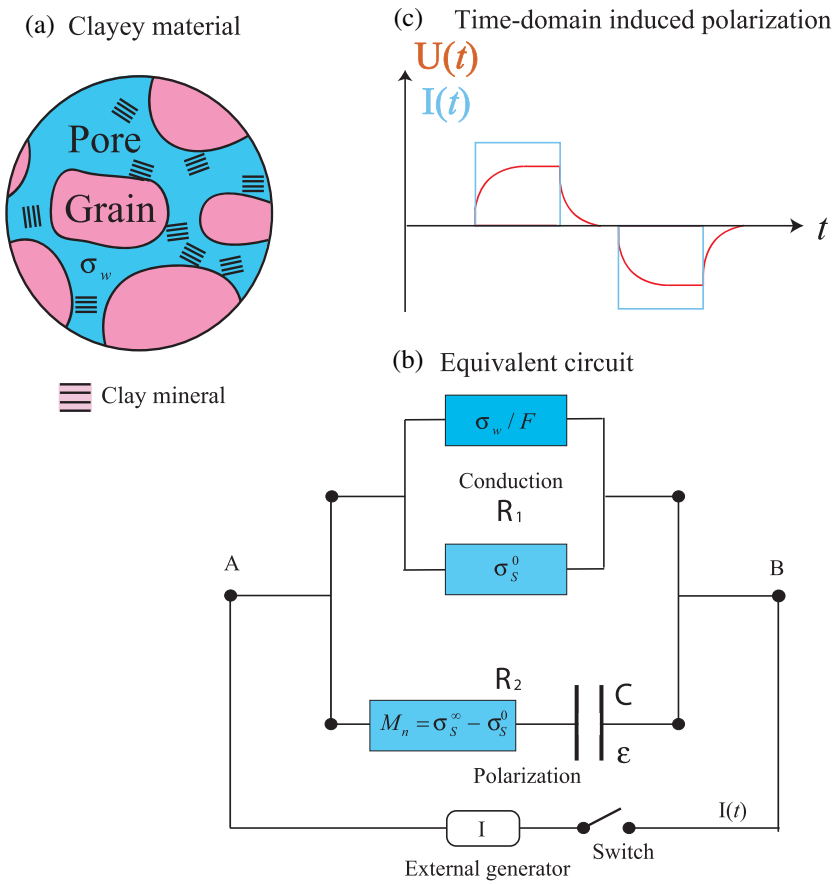

Figure 3. Polarization of a granite. (a) The presence of clay minerals in the granite (because of its alteration) has a drastic effect in time-domain-induced polarization since, because of their small sizes, they are the first grains to get fully polarized in an applied electrical field. (b) Equivalent electrical circuit with a resistance R_1 (conduction in pore space and diffuse layer) in parallel with a resistance R_2 (conduction in the Stern layer) in series with a capacitance C representing the capacitance of the grains. The presence of the electrical double layer coating the surface of the grains has an effect on both conduction and polarization. It controls directly the occurrence of (induced) polarization. (c) Time-lapse response of the equivalent circuit. Time-domain-induced polarization is based on this principle with a box current (strength I) characterized by a period generally comprised between 0.1 and 10 s. In this paper, we use a period of 1 s. Note that the apparent normalized chargeability determined from the first window of the decay curves for the secondary voltage depends on the period used for the current injection.

(Stern 1924) while the diffuse layer contains counterions and co-ions connected to the surface charge density through only the Coulombic force (Gouy 1910). A petrophysical model based on the so-called dynamic Stern layer model (e.g. Rosen *et al.* 1993; Leroy *et al.* 2008; Revil 2013a, b) can be used to obtain images of the water content, cation exchange capacity (CEC) or specific surface area of the porous material and permeability of the subsurface (Revil & Gresse 2021).

The self-potential method is a passive geoelectrical technique sensitive to groundwater flow (Sill 1981, 1983; Soueid Ahmed *et al.* 2013; Revil *et al.* 2017). As pointed out above, the grains of a porous material are surrounded by the electrical double layer. The flow of the pore water drags part of the excess of electrical charge of the diffuse layer located in the pore space generating a source of electrical current. There is a so-called shear plane where the relative difference of the velocity between the fluid phase relative to the solid phase is null. The part of the diffuse layer located beyond this shear plane inside the pore space is susceptible to be dragged by the flow of the pore water. In turn, this source of current generates electromagnetic disturbances through the porous material. These electromagnetic disturbances can be remotely measured and inverted to characterize groundwater flow (Revil & Jardani 2013; Rittgers *et al.* 2015; Soueid Ahmed *et al.* 2016). A self-potential map is a map of the electrical potential distribution obtained at the ground surface with a voltmeter (input impedance > 10 MΩ; sensitivity of 0.1 mV) with respect to a point called the reference (a fixed electrode corresponding to a zero electrical potential from which the self-potential anomalies are considered, see Revil & Jardani 2013).

The self-potential anomalies can be inverted using geophysical methods developed in the realm of potential field techniques in hydrogeophysics (Revil & Jardani 2013; Shamsipour *et al.* 2013), volcanology (Kuwano *et al.* 2015) and ElectroEncephaloGraphy (EEG) in medical imaging (Grech *et al.* 2008). Regarding EEG, there is a lot knowledge to be gained from EEG imaging and to be transferred in the inversion of self-potential data. Groundwater flow pattern (Darcy-velocity distribution) can be recovered at any scale as discussed by Revil & Jardani (2013), and references therein.

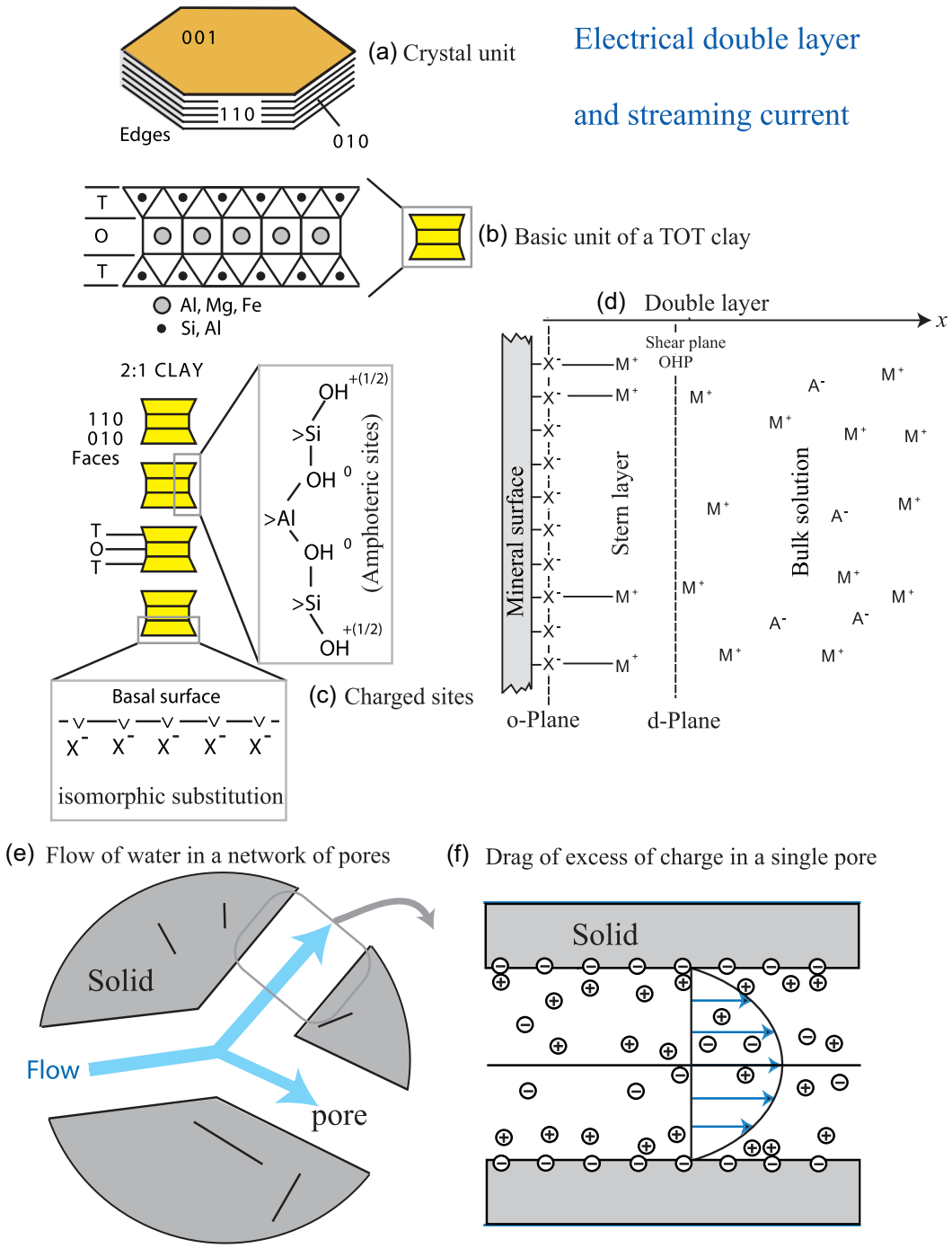

Figure 4. Underlying physics of the streaming current. (a) A clay crystal is characterized by different crystalline planes that are charged through two different mechanisms (acid/base reactions and isomorphic substitutions). (b) Sketch of the TOT structure of a clay mineral like smectite with T the tetrahedral layer based on the chemistry of silicium Si (with possible isomorphic substitution with aluminium Al) and O the octahedral layer based on the chemistry of aluminium (with possible isomorphic substitution with magnesium Mg and iron Fe). (c) The sites on the clay crystal edges are usually amphoteric sites (i.e. the charge is pH-dependent) and charges associated with isomorphic substitutions on the basal planes (which are pH-independent). (d) The electrical double layer is formed by the Stern layer of sorbed counterions and the diffuse layer. (e) Flow of water in the pore space. (f) Streaming current density j_S produced by the drag of the mobile excess of charge located in the pore space by the flow of the pore water.

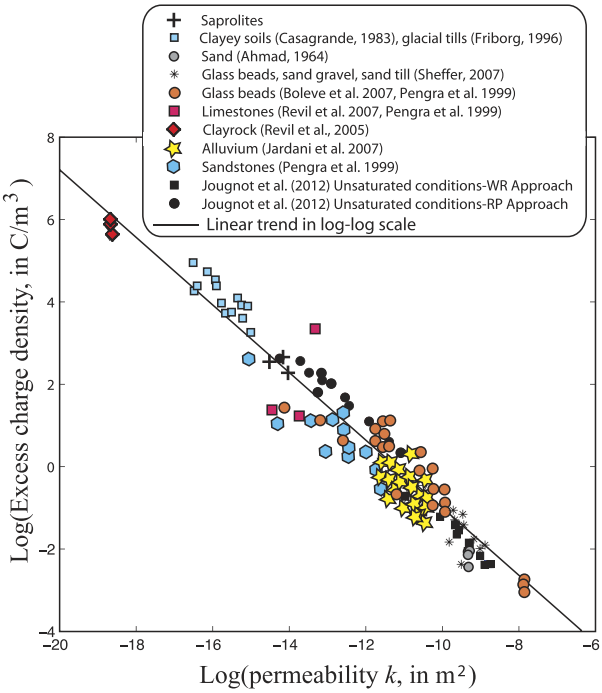

Figure 5. Plot of the effective charge density (in C m^{-3}, see Appendix A) versus permeability (in m^2). The trend is obtained using a broad collection of cores displaying various lithologies. This indicates the universal character of the trend. The pore water are characterized by near neutral pH values ($5 < \text{pH} < 8$). The data are from Ahmad (1969), Casagrande (1983), Friborg (1996), Pendra et al. (1999), Revil *et al.* (2005b, 2007), Jardani *et al.* (2007), Sheffer (2007), Bolève *et al.* (2007b) and Jougnot *et al.* (2012). The variations cover 10 decades in excess charge density and permeability.

Other mechanisms of subsurface source current densities are possible. For instance, the membrane polarization results from the presence of a salt concentration gradient (Maineult *et al.* 2006) and the thermoelectric effect is associated with the presence of a temperature gradient (e.g. Revil 1999). In addition, the (bio-)geobattery mechanism has been observed in presence of a biotic or abiotic electronic conductors crossing areas of different redox potentials (Revil *et al.* 2023a). That said, in most cases, in absence of metallic body, the electrokinetic conversion mechanism associated with ground water flow is dominant (Revil & Jardani 2013).

Since induced polarization is sensitive to permeability and self-potential is sensitive to the Darcy velocity, they can be naturally combined to get more insights into groundwater flow. This is the task of this paper to provide a road map in this direction with a specific application to the detection and quantification of groundwater flow downstream from a dam in a granitic substratum. More precisely, the application made in the present paper is to characterize groundwater flow below the dam of Lampy localized near the city of Carcassonne in the Black Mountain (Aude) in south-central France (Figs 1 and 2).

The Lampy reservoir was created in 1782 after four years of work in building a dam closing the Lampy Valley (Black Mountain, Aude, France). The resulting reservoir (∼1 500 000 m^3) was built to provide a water source for the Canal du Midi. The idea was originally proposed in 1665 by the French Engineer Pierre-Paul Riquet following the work by a commission created by Louis XIV, King of France. After the completion of the dam and the infilling of the reservoir, numerous leaks in the dam itself and in the granitic substratum were evidenced. The dam and the underlying formation were efficiently sealed by pouring a large quantity of quick lime into the reservoir. Until nowadays, the dam is considered to be very safe with little evidences for leaks. However, a spring is observed since 2022 at the downstream toe of the dam and an area downstream the dam is characterized by a saturated soil. Our study investigates the pattern of groundwater flow just downstream the dam.

2. TOWARD A NON-INTRUSIVE GROUND FLOW SENSOR

2.1. Induced polarization

Induced polarization method is an active geophysical method looking at imaging the electrical conductivity and the normalized chargeability of the subsurface (the normalized chargeability is defined as the difference between the instantaneous conductivity and the DC, direct current, conductivity of the rock, this difference reflecting the phenomenon of low-frequency polarization). In principle, the conductivity, the normalized chargeability, and the permeability of a rock are interrelated second-order symmetric tensors. (see Revil *et al.* 2023b). If permeability is anisotropic, the complex conductivity is also anisotropic, which may be the case in granite. That said, in practice, it may be difficult to separate what is related to heterogeneity and what is related to anisotropy. To keep things simple, we consider below that the rock is isotropic.

The presence of clay minerals in granite (especially kaolinite) is responsible for surface conductivity (conductivity associated with the double layer of the clay minerals) and polarization (Bremer et al., 1992). This makes the rock behaving as an RC circuit as shown in Fig. 3. The resistance $R1$ is essentially associated with conduction in the bulk pore water occurring in parallel to the conduction in the electrical double layer along the grains in contact with the bulk pore space. The resistance $R2$ is associated with the excess conductivity associated with conduction in the Stern layer at high frequencies. The capacitance C is due to the polarization of the grains at low frequencies. Indeed, the separation of the charges across the grain scale at low frequencies implies that the grains are giant dipoles at these frequencies. At high frequencies, the grains have no time to polarize. In time-domain-induced polarization, the period used to inject the primary current dictates what polarization length scales will get polarized. For instance for a period of 1 s (usually used in field investigations), only the clay minerals are expected to get polarized, not the large grains.

According to the dynamic Stern layer model and using harmonic current excitations behaving as $\exp(-i\omega t)$ (t is time, in s, and ω denotes the angular frequency in rad s^{-1}), Ohm's law and the complex conductivity $\sigma*(\omega)$ of such porous material are given by (e.g. Revil 2013a, b; Revil *et al.* 2017)

13

$$\mathbf{j}(\omega) = \sigma*(\omega)\mathbf{E}(\omega), \tag{1}$$

$$\sigma*(\omega) = \sigma_\infty - M_n \int_0^\infty \frac{h(\tau)}{1-(i\omega\tau)^{1/2}} \mathrm{d}\tau, \tag{2}$$

respectively, where $\mathbf{j}$ (A m^{-2}) and $\mathbf{E}$ (V m^{-1}) denote the current density and electrical field, respectively, τ (s) is a time constant (also called a relaxation time since corresponding to a diffusion process), $h(\tau)$ denotes the (normalized) probability density associated with the distribution of the time constants of the material (in turn related

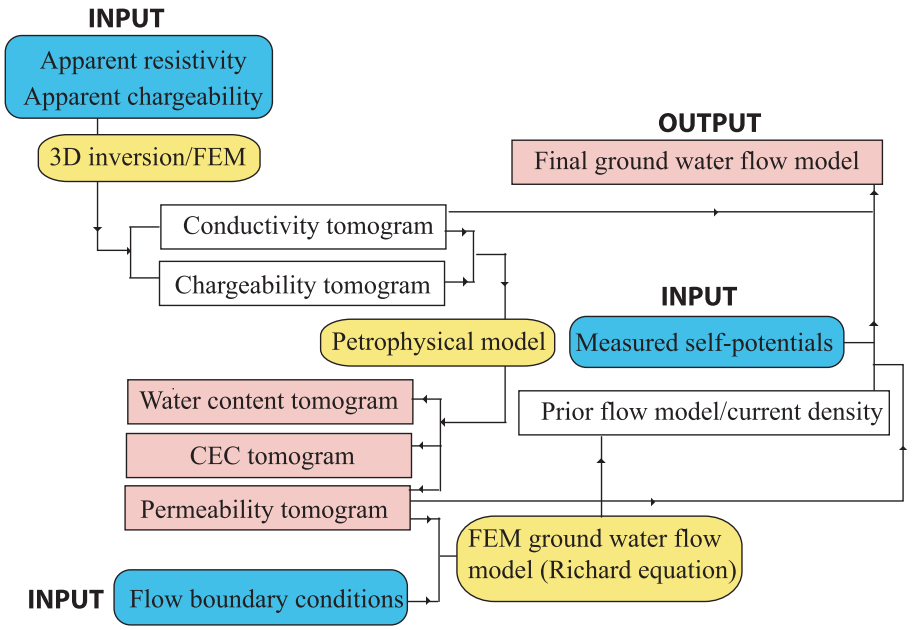

Figure 6. Flowchart used to determine the groundwater flow model using a combination of electrical conductivity, normalized chargeability (obtained from inversion from the product cell-by-cell of the chargeability by the conductivity) and self-potential data. FEM stands for finite-element method. The induced polarization method is used to determine the permeability distribution, which with appropriate boundary conditions, is used to define a prior groundwater flow model. Thanks to the electrical conductivity and self-potential data, this prior groundwater flow model is updated into a posterior groundwater flow model.

to its distribution of polarization length scales), $M_n = \sigma_\infty - \sigma_0$ (S m^{-1}) is the normalized chargeability, and σ_0 and σ_∞ (expressed in S m^{-1}) denote the DC (direct current, ω=0) and high-frequency (instantaneous) electrical conductivities, respectively. The use of the ½ exponent in the kernel of the complex conductivity (Warburg distribution) is explained in details in Revil (2013a, b) and Revil *et al.* (2017) and associated with the leaking character of the double layer capacitance in the induced polarization of insulating grains coated by an electrical double layer.

Using Archie's (1942) law extended to the relationship between the formation factor and the water content, the expressions of these two conductivities are (Revil 2013a, b),

$$\sigma_0 = \theta^m \sigma_w + \theta^{m-1} \rho_g (B - \lambda) \mathrm{CEC}, \tag{3}$$

$$M_n = \theta^{m-1} \rho_g \lambda \mathrm{CEC}. \tag{4}$$

In these equations, θ (dimensionless) denotes the liquid pore water content (vol. fraction), and CEC denotes the cation exchange capacity of the material (expressed in C kg^{-1} or alternatively in meq per 100 g with 1 cmol kg^{-1} = 1 meq per 100 g = 963.20 C kg^{-1} in SI units), $\rho_g \approx$ 2700 kg m^{-3} is the mass density of the grains, σ_w (in S m^{-1}) denotes the pore water conductivity, $m > 1$ (dimensionless) is called the porosity or first Archie's exponent, the mobility B (in m^2 s^{-1} V^{-1}) denotes the apparent mobility of the counterions for surface conduction, and λ (in m^2 s^{-1} V^{-1}) denotes the apparent mobility of the counterions for the polarization. A dimensionless number R is also introduced as $R = \lambda / B$ and with $B(\mathrm{Na}^+, 25\,^\circ\mathrm{C}) = 3.1 \pm 0.3 \times 10^{-9}$ m^{-2} s^{-1} V^{-1} and $\lambda(\mathrm{Na}^+, 25\,^\circ\mathrm{C}) = 3.0 \pm 0.7 \times 10^{-10}$ m^{-2} s^{-1}V^{-1}, we have $R \sim 0.10 \pm 0.02$ (independent of saturation and temperature). In saturated conditions, the exponent m can be considered to be the cementation exponent of the old literature but with the warning that m has nothing to do with a cementation process.

In field conditions, induced polarization tomography can be used to obtain 3-D images/tomograms of the electrical conductivity and normalized chargeability distributions thanks to an impedance meter, cables and stainless steel electrodes. Then, we can obtain the water content θ and the CEC by solving eqs (3) and (4) (two observations and two equations for two unknowns) for each element of the tomogram to obtain the distributions (tomograms) of θ and CEC. Since we have two equations with two unknowns, we obtain:

$$\theta \approx \left[\frac{1}{\sigma_w} \left(\sigma_\infty - \frac{M_n}{R} \right) \right]^{1/m}, \tag{5}$$

$$\mathrm{CEC} = \frac{M_n}{\theta^{m-1} \rho_g \lambda}, \tag{6}$$

and we consider at a very good approximation that the conductivity at a given frequency is close to the instantaneous conductivity in eq. (5). In eqs (5) and (6), we need to know the conductivity of the ground water (from the TDS, total dissolved solid of the water in a well or a spring) and the grain density of the solid grain ρ_g ($\approx$2700 kg m^{-3} for silicates and aluminosilicates). Once we have the water content θ and the CEC, we can image the permeability k (expressed in m^2) of the subsurface using (Soueid Ahmed *et al.* 2020b)

$$k \approx \frac{k_0 \theta^6}{\left(\rho_g \mathrm{CEC} \right)^2}, \tag{7}$$

with $k_0 = 10^{4.30}$ in SI units (C^2 m^{-4}), θ is unitless and the CEC is here expressed in C kg^{-1}. Example of the quantitative evaluations of the induced polarization for localizing leaks in dams and

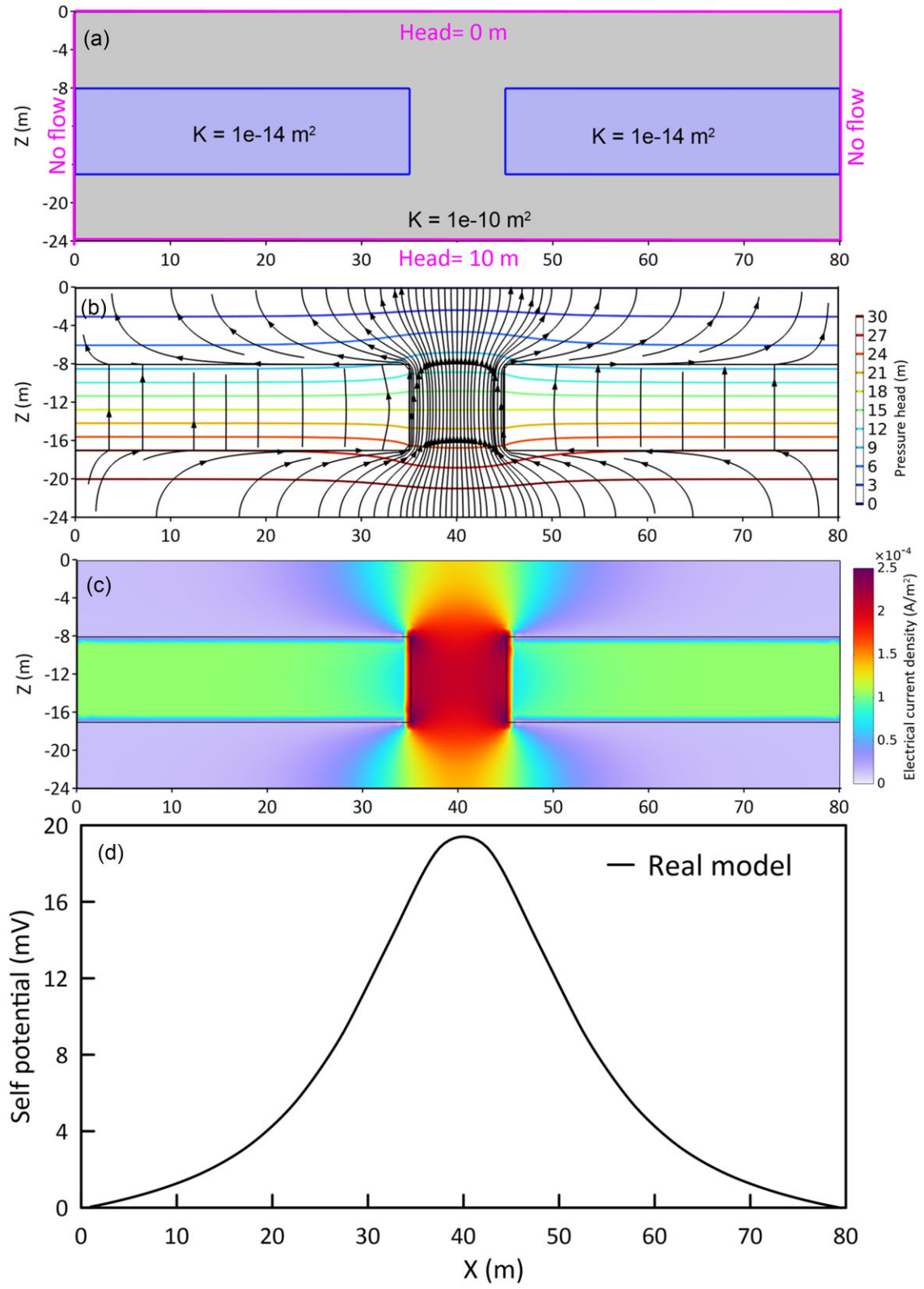

Figure 7. Direct problem of self-potential for the real model. (a) A 2-D heterogeneous permeability model contains two layers permeable and relatively non-permeable. The boundary conditions for the lateral edges is no flow and un difference of 10 m in pressure head for two lower and upper edges. (b) Pressure head (plain lines) and Darcy velocity (arrow lines). (c) *z*-component of the source current density. (d) Self-potential at the ground surface.

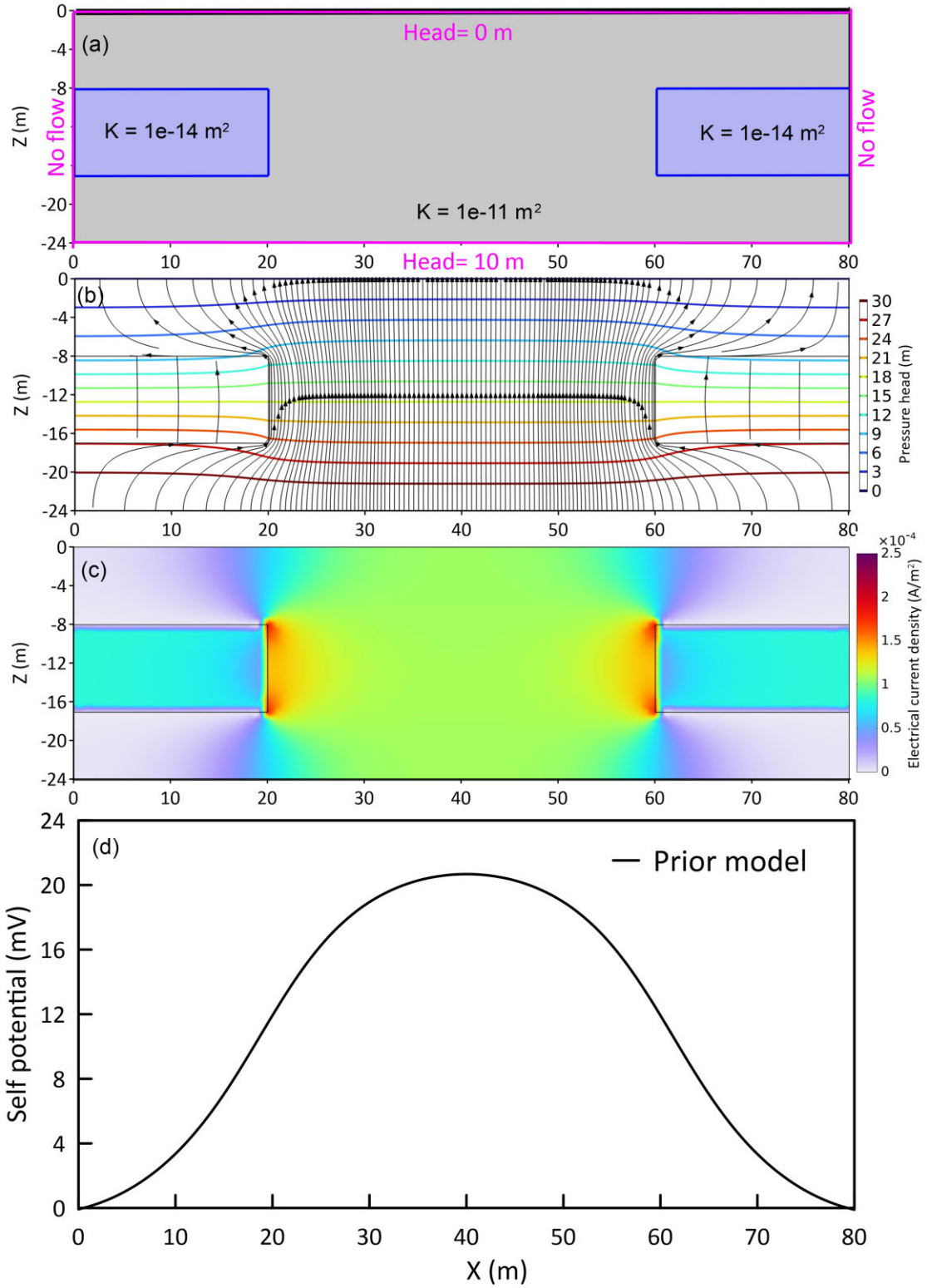

Figure 8. Direct problem of the self-potential for a prior ground water flow model. (a) The 2-D heterogeneous permeability model contains two layers permeable and relatively non-permeable. The boundary conditions for the lateral edges is no flow and un difference of 10 m in pressure head for two lower and upper edges. (b) Pressure head (plain lines) and Darcy velocity (arrow lines). (c) The *z*-component of the external current density. (d) Resulting self-potential at the ground surface.

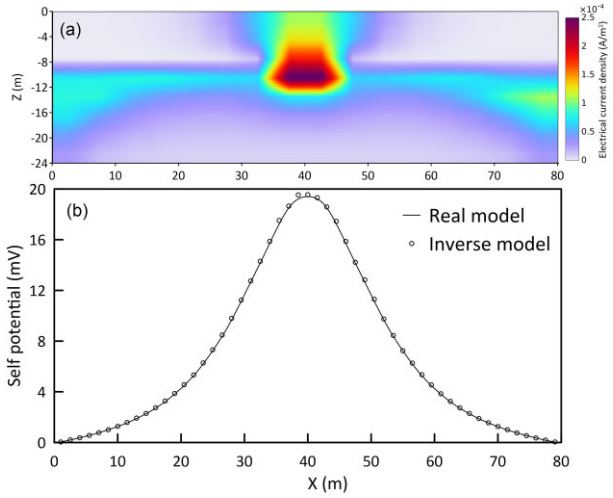

Figure 9. Results of the inversion process. (a) Recovered electrical current density in the vertical direction. Note that the inverse problem is able to recover both the location and the magnitude of the anomalous current density associated with ground water flow. (b) Comparison between the true self-potential distribution and the fit corresponding to the optimized solution of the inverse problem.

embankments can be found in Abdulsamad *et al.* (2019), Soueid Ahmed *et al.* (2020b), 2023) and Ghorbani *et al.* (2023).

2.2. The self-potential method

The self-potential method is a passive electrical method recording the electrical field/potential at the ground surface of the Earth or at the seafloor (Su *et al.* 2022). The resulting self-potential map (or its fluctuations over time) can be related to the occurrence of source current densities in the subsurface (Revil & Jardani 2013). The method is similar in essence to EEG in medical imaging for which the sources of current are generally located at the synapses between the neurons (Merlet & Gotman 2001). While a variety of mechanisms can be responsible for the causative current source of self-potential signals in Earth sciences, in absence of ore deposits, the main mechanism is assumed to be the so-called electrokinetic mechanism associated with groundwater flow (Revil & Jardani 2013). The flow of the pore water drags the excess of charge contained in the electrical double layer coating the surface of the grains. Its results in a source current called the streaming current density (Fig. 4). In turn, this source current density generates low-frequency electromagnetic disturbances that can be remotely recorded (see Fig. 4; Rittgers *et al.* 2015).

The underlying physics is pretty simple. In isotropic porous media and assuming that the fluctuations in the pore water flow are slow enough, the total current density $\mathbf{j}$ ($\mathrm{A\,m^{-2}}$) is the sum of two contributions one associated with conduction and one associated with advection (see Sill 1981, 1983; Revil & Jardani 2013):

$$\mathbf{j} = \sigma_0\, \mathbf{E} + \mathbf{j}_s. \tag{8}$$

In eq. (8), σ_0($\mathrm{S\,m^{-1}}$) denotes the DC electrical conductivity of the porous material, the first term $\sigma_0\mathbf{E}$ represents the conductive current density originating from the electromigration of ions in the porous material, $\mathbf{E}$ denotes the electrical field and $\mathbf{j}_s$ denotes the streaming (source) current density (see Revil & Gresse 2021, and references therein).

In the quasi-static limit of the Maxwell equations, $\nabla \times \mathbf{E} = 0 \Rightarrow \mathbf{E} = -\nabla\varphi$, where φ denotes the electrical potential (in V). Bolève *et al.* (2007a) write the streaming current density as the product of an effective excess of charge in the pore water and the Darcy velocity (e.g. Revil & Jardani 2013): 14

$$\mathbf{j}_S = \hat{Q}_V(s_w)\dot{\mathbf{w}}, \tag{9}$$

where $\dot{\mathbf{w}}$ denotes the filtration velocity (Darcy velocity in $\mathrm{m\,s^{-1}}$, i.e. the flux density of the pore water in saturated or unsaturated conditions) and $\hat{Q}_V$ denotes the effective excess charge density associated with the advection of the diffuse layer in $\mathrm{C\,m^{-3}}$ with $\log_{10}\hat{Q}_V(s_w = 1) = -9.2 - 0.82\log_{10}k$ (see Fig. 5 and Appendix A) where k denotes the permeability in $\mathrm{m^2}$. The Darcy velocity corresponds to time derivative of the volume-averaged filtration displacement $\mathbf{w} = \theta(\mathbf{u_w} - \mathbf{u})$ where s_w denotes the water saturation ($s_w = 1$ at saturation), and $\mathbf{u_w}$ and $\mathbf{u}$ the water phase and solid displacements, respectively (see Jardani *et al.* 2010, for further details). In the quasi-static limit of the Mawxell equations, the conservation equation for the total current density is given by,

$$\nabla \cdot \mathbf{j} = 0. \tag{10}$$

Combining the conservation equation with the constitutive equation leads to a Poisson equation for the self-potential field φ (see Sill 1981, 1983; Revil & Jardani 2013)

$$\nabla^2\varphi = -\nabla \ln\sigma_0 \cdot \nabla\varphi + \frac{1}{\sigma_0}\nabla \cdot \left(\hat{Q}_V\dot{\mathbf{w}}\right). \tag{11}$$

Eq. (11) shows that the self-potential anomalies are modulated by the distribution of the electrical conductivity (secondary sources, first term of the right-hand side of eq. 11) in addition to the groundwater flow itself (primary source, last term of the right-hand side of eq. 11). It follows that to invert self-potential signals, the electrical conductivity tomogram needs to be used to distinguish primary and secondary sources (see recently Su *et al.* 2022). As a side note, the electrokinetic properties of granite are discussed in Ishido & Mizutani (1981) and are similar to other silicate-based rocks.

In identifying the causative sources of self-potential signals, care should be taken since self-potential anomalies can be also associated with certain redox potential distribution and biotic or metallic electronic conductors (see Revil *et al.* 2001; Linde & Revil 2007; Castermant *et al.* 2008). Generally, the self-potential anomalies associated with metallic bodies are negative and rather large (−500 mV to −1 V in amplitude).

2.3. Combined approach

Recovering directly the Darcy velocity from a self-potential map is a difficult task because of the non-unicity of the inverse problem, which is notorious in the realm of potential-field inverse problems. The idea underlying the present approach is that a prior model for the Darcy velocity (hence the current density) can be generated using the permeability distribution obtained from the induced polarization data. In short, we generate a meaningful flow model that is converted into a prior source current density distribution. This prior source current density distribution is updated thanks to the self-potential data into a posterior source current density distribution, which is in turn converted into an updated groundwater flow model. The inversion of the self-potential data is done with the Gauss Newton approach as suggested by Revil & Jardani (2013). The flow chart we follow in this paper in combining electrical conductivity, normalized chargeability, self-potential and boundary conditions for the flow

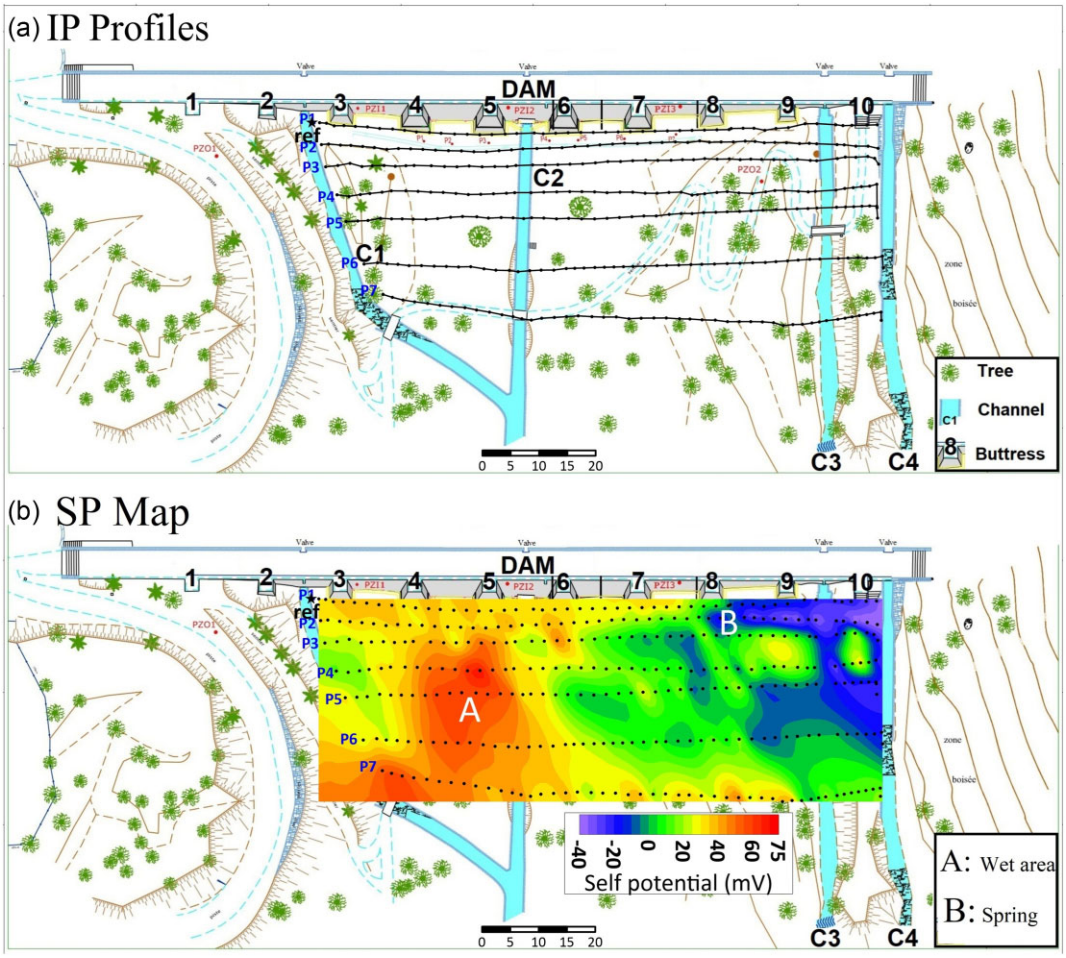

Figure 10. Position of the geophysical survey**.** IP and SP stand for induced polarization and self-potential, respectively. (a) Position of the seven profiles used to perform the 3-D reconstruction of the conductivity and normalized chargeability and crossing the valley downward the dam of Lampy. The profiles are labelled P1–P7. The sketch shows the position of the tress as well as the position of the dam and the four channels downstream. (b) Self-potential map in mV (337 SP stations are covered in the survey along the same seven profiles used for the resistivity/induced polarization survey). Ref denotes the reference point (zero potential) for the self-potential map. This indicates where the reference electrodes has been placed during the survey. The area A corresponds to an area where the ground is wet, while B characterizes a spring at the foot of buttress 8. The elements C1, C2, C3 and C4 denote four channels located downstream and used to control the outflow of water from the dam. The scale is in metres.

of the ground water is summarized in Fig. 6. It is obvious that the posterior flow model could be biased by the prior model. For instance, in the present case study, we will not be interested by a shallow ground water flow coming from the side of the test site in order to focus on the ground water flow passing below the dam in some fractured granite.

2.4. Synthetic test validation of the self-potential inversion algorithm

We check now the algorithm used to invert the self-potential data (see Appendix B) using a 2-D case (see Figs 7–9). We consider a vertical 2-D cross-section with the dimensions 80×24 m^2. We first simulate Darcy flow with the hydraulic model shown in Fig. 7 using Comsol multiPhysics. The flow equation is solved in the saturated case in steady state. An impervious boundary condition on the two vertical sides and a head gradient imposed on the lower and upper layers are considered for this simulation. The pressure heads (colour lines) and the Darcy velocity distribution (arrow lines) are shown in Fig. 7(b). Then, we compute the source electrical current density ($\mathbf{j}_s$, in A m^{-2}) using the relationship between the Darcy velocity and the source current density, see eq. (9), as well as the relationship between the effective charge density at saturation and the permeability. Finally, we solve eq. (11) for the electrical potential (insulating ground boundary condition and potential going to zero at infinity). Fig. 7(c) shows the source current density in the z-(vertical) direction and the self-potential (expressed in mV) is shown in Fig. 7(d).

Now the goal of the inversion algorithm is to use the self-potential data simulated at the ground surface and a prior source current density associated with a prior ground water flow problem. For the inverse problem, we used the method developed by Soueid Ahmed *et al.* (2013) and summarized in Appendix B. The prior model is presented in Fig. 8 and is determined from the following prior ground water flow model shown in Fig. 8. The permeabilities and the geometry of the subsurface layers are different (on purpose) from the true model (compare Figs 7 and 8) and in order to use a prior model that

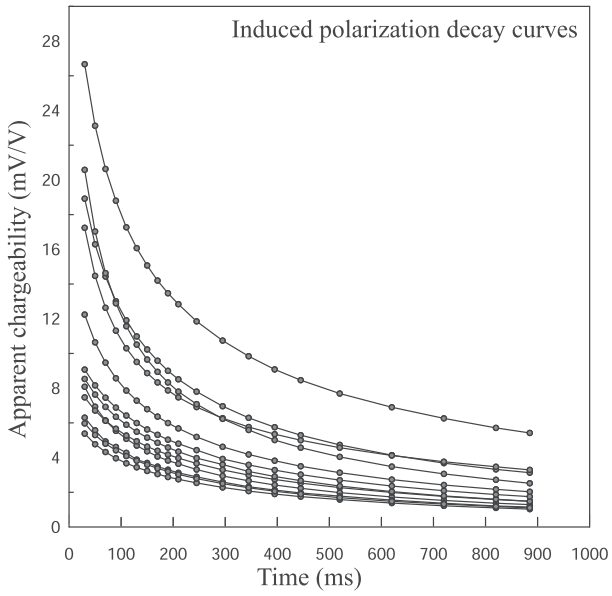

Figure 11. Examples of time-induced polarization decay curves for the apparent chargeability (expressed in mV V^{-1}) showing the high quality of the induced polarization data. The fact that the potential difference between the voltage electrodes M and N decays steadily to zero indicates that the ground is polarized under the influence of the primary electrical field imposed through the current injected between the electrodes A and B. The apparent chargeabilities are obtained by integrating over time the voltage decay curve (first black dots in time). We use the first time window to obtain the apparent chargeabilities used in the inversion model. We do not observed electromagnetic coupling effects in the secondary voltage data.

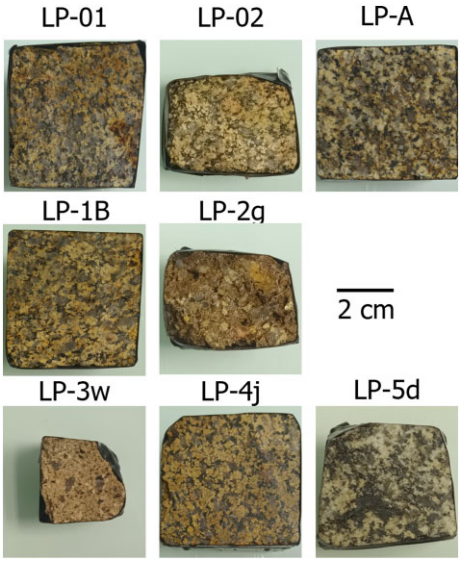

Figure 12. Pictures of the eight core samples used for the laboratory investigations. The samples have collected at outcrops downstream the Lampy reservoir. Their petrophysical properties (electrical characteristics, porosity and CEC) are reported in Table 1.

Table 1. Petrophysical properties of the eight core samples collected at the test site. The CEC is expressed in meq per 100 g (1 meq per 100 g = 963.20 C kg^{-1} in SI units) and measured using the cobalt hexamine method. The surface conductivities and formation factors are determined by plotting the conductivity of the material (at 10 Hz) as a function of the pore water conductivity. The normalized chargeability M_n is computed from the difference of the in-phase conductivity between 100 mHz and 1 kHz. The in-phase and quadrature conductivities are reported at 10 Hz and for a pore water conductivity of 0.0312 S m^{-1} at 25 °C.

Full name	Porosity ϕ (−)	CEC (meq per 100 g)	F (−)	σ_S (10^{-4} S m^{-1})	M_n (10^{-4} S m^{-1})	σ' (10^{-4} S m^{-1})	σ'' (10^{-6} S m^{-1})
LP-01	0.06	2.12	139 ± 3	1.3 ± 0.1	0.37	1.54	2.23
LP-1B	0.07	3.15	118 ± 4	8.8 ± 1.2	0.57	3.43	5.21
LP-02	0.16	2.92	24 ± 0.1	10.5 ± 2.6	1.71	25.2	1.65
LP-2g	0.27	4.01	18 ± 1	13.2 ± 5.0	1.04	14.0	8.79
LP-3w	0.65	14.0	2.2 ± 0.5	92 ± 10	22.7	231	164
LP-4j	0.08	2.97	126 ± 1	6.5 ± 0.9	0.54	5.58	5.31
LP-5d	0.08	1.60	61 ± 2	5.4 ± 3.7	0.25	4.79	2.66
LP-A	0.05	2.13	255 ± 3	2.2 ± 1.0	0.25	1.30	1.72

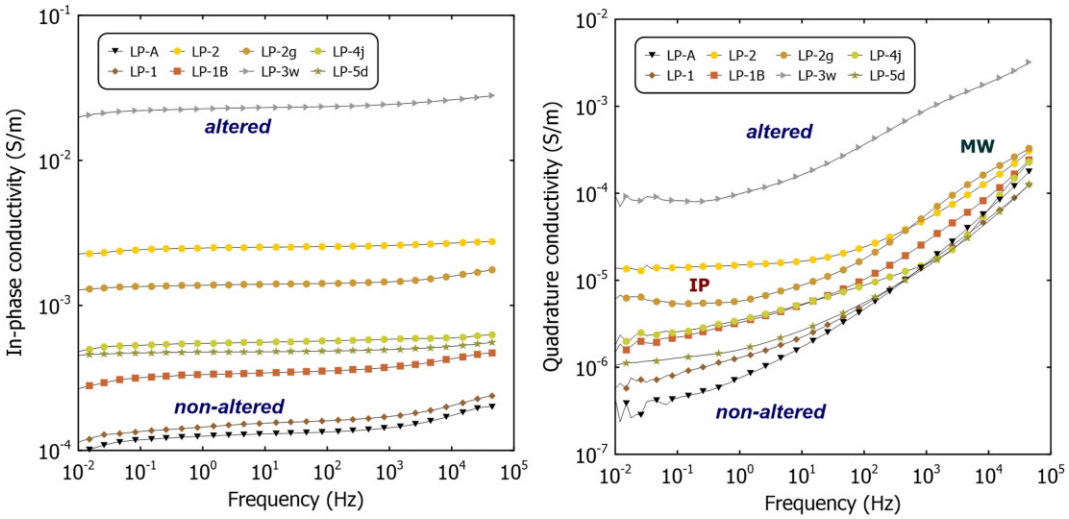

Figure 13. Complex conductivity spectra for the eight core samples used for the laboratory investigations at 0.1 S m^{-1}. IP stands for induced polarization (i.e. related to electrical double layer polarization) and MW for Maxwell–Wagner polarization (i.e. related to the discontinuity of the displacement current at the interface of the phases forming the porous composite). For the less altered core samples, the IP effect is dominant only below 100 Hz. The pore water conductivity is 0.0312 S m^{-1} (NaCl, 25 °C).

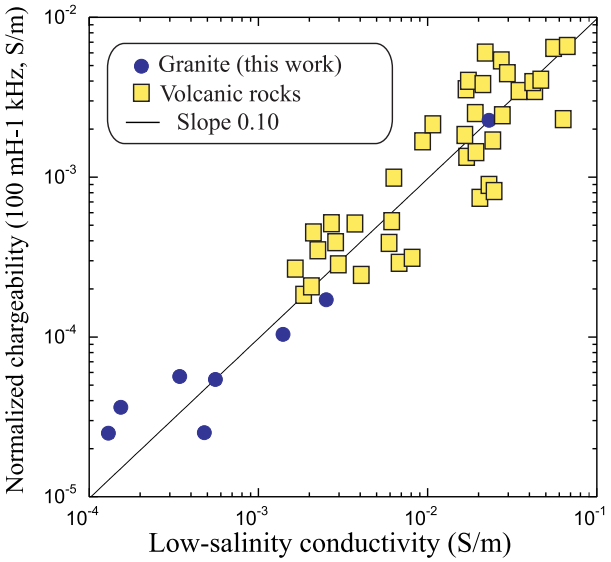

Figure 14. Normalized chargeability versus low-salinity conductivity (0.03 S m^{-1}, NaCl, 10 Hz, close to the surface conductivity). The normalized chargeability is determined form the domain in which the IP effect is dominant (below 1 kHz). When surface conductivity dominates the conductivity response, the normalized chargeability and the conductivity are expected to be highly correlated with $M_n = R\,\sigma'$. The presence of pyrite would break such trend (see discussion in Revil *et al*. 2021). The granitic rocks are from Lampy (kaolinite-rich), while the volcanic rocks (smectite-rich) are from the La Soufrière stratovolcano (Guadeloupe island, see Zhang *et al.* 2023).

is physically meaningful but inaccurate in terms of ground water flow model. Fig. 9 shows the retrieved current density in the vertical direction and compare the ground surface self-potential distribution of the true model (Fig. 7) and the self-potentials distribution associated with the of source current density obtained from the inverse model. The inverted current density anomaly (Fig. 9b) shows the position and the strength of the source current density associated with the ground water flow.

3. FIELD AND LABORATORY INVESTIGATIONS

3.1. The dam of Lampy

The dam of Lampy is located in the South of France, in the Aude department, between the cities of Toulouse and Carcassonne (Fig. 1). The dam is managed by Voies Navigables de France (VNF) and it constitutes an element of the Black Mountain hydraulic development system. The structure has been built between 1778 and 1782 in order to supply the Canal du Midi in water over the year. It is therefore an old dam, declared as an UNESCO world heritage site.

The Lampy dam is a gravity (masonry) dam, reinforced with 10 buttresses (see Figs 1 and 2). It is composed of granite rubble stones, bound with lime mortar. The dam stands ∼18 m high above its foundation. Its length is close to 140 m and its width is 5.5 m at the crest. The reservoir contains ∼1.5 million of cubic metres at the normal operating level. The foundation is composed of sound granite at the banks but the granite is much more altered at the bottom of the valley, with the presence of granitic sands, resulting from the desegregation of the granite substratum.

Initially, the dam did not include a drainage system. Renovation and reinforcement works were carried out in 2016. To limit the pore water pressures under the structure, 10 drains have been drilled into the dam from the downstream face and a drainage trench has been dug at the downstream toe of the dam, along with 7 relief wells. The overall stability was also enhanced by the installation of 13 active anchors on the crest of the dam. The dam is monitored with 15 pore pressure cells placed within the masonry and at the contact between the dam and the foundation, 2 open piezometers, 20 seepage measurements at the downstream toe

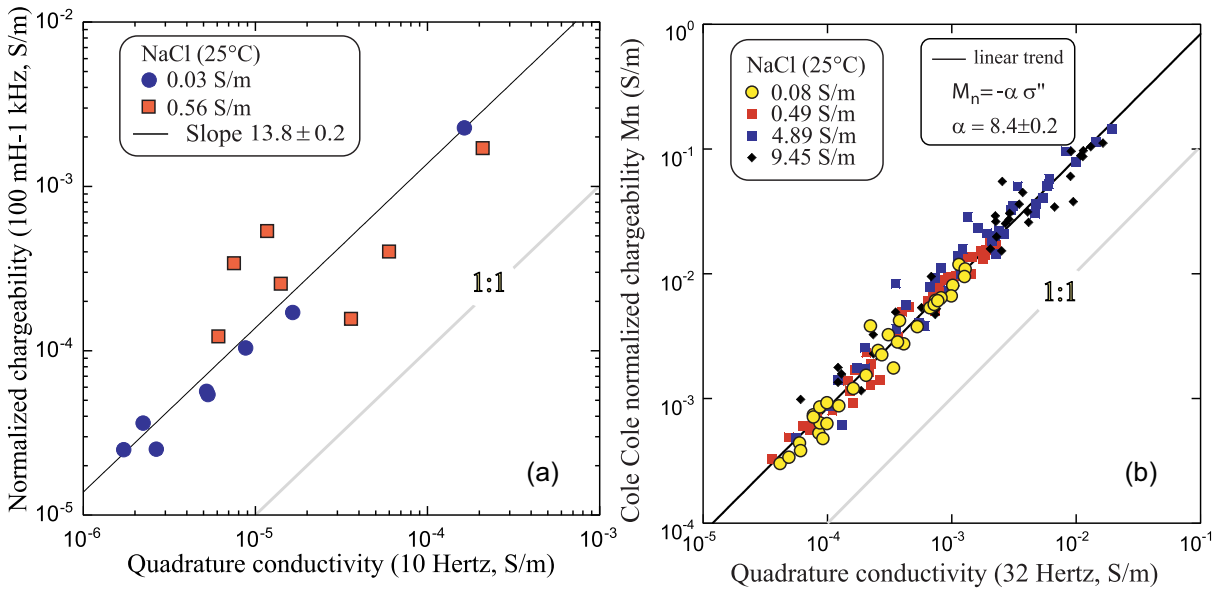

Figure 15. Normalized chargeability versus quadrature conductivity. (a) Granitic samples (0.03 $S\,m^{-1}$, NaCl, 10 Hz). The normalized chargeability is determined form the domain in which the IP effect is dominant as the difference between the in-phase conductivity between 0.1 Hz and 1 kHz. The quadrature conductivity is taken at the geometric mean of the two frequencies (i.e. 10 Hz). Both the dispersion of the in-phase conductivity with frequency and the quadrature conductivity represent the same IP polarization process. (b) Volcanic rocks from the study of Zhang *et al.* (2023). Core samples from La Soufrière stratovolcano (Guadeloupe Island).

of the dam, two crack detectors and 6 measurements of anchors strength.

In 2022 March, a small spring appeared on the buttress 8 level. The flow rate has since been measured on a weekly basis with an outflow comprised between 0.6 to 1.5 $l\,min^{-1}$ when the spring is active (Fig. 2). This spring seems however to originate from the side of the valley, possibly associated with one of the channel used to evaluate excess water from the reservoir and is therefore not of crucial interest in the present study.

3.2. Geophysical survey

The geophysical survey was done in 2023 Spring. It consisted of seven electrical conductivity/induced polarization profiles (Fig. 10a) performed with the 20-channel TERRA impedance meter from IRIS (http://www.iris-instruments.com/in-product.html) and one cable of 48 electrodes (electrode spacing of 2 m, 360–365 measurements per profile with a total 2516 measurements for the conductivity and the chargeability for the 3-D inversion). We use the Wenner configuration and the time-domain measurements were done using the following acquisition characteristics: 1 s for the primary current injection between the electrodes A and B, a dead time of 20 ms and the apparent chargeabilities measured on 20 windows (windows 1–10 have a duration of 20 ms, windows 11–15 have a duration of 50 ms and finally windows 16–20 have a duration of 100 ms, see Fig. 11 for some examples of the decay of the apparent chargeabilities). The decay curves in Fig. 11 show exponential-like decays indicating a high degree of confidence into the data quality. The Wenner configuration was chosen for its high signal-to-noise ratio. Wenner array is generally sensitive to EM coupling for induced polarization measurements, especially when multi-electrodes cable is used. Fig. 11, however, does not exhibit any evidence of electromagnetic coupling effects, which is likely confined inside the dead time used for the survey (see an extensive discussion in Mao *et al.* 2016).

In addition, we perform a self-potential survey using two non-polarizing $Pb/PbCl_2$ electrodes. The voltage measurements are taken with a high input resistance voltmeter (100 MΩ) and a sensitivity of 0.1 mV. The survey comprises 336 stations in the area covered by the conductivity/induced polarization survey. A map of the self-potential survey is shown in Fig. 10(b). This map corresponds to the distribution of the measured electrical potential difference with respect to a reference electrode (fixed, see 'ref' in Fig. 10b). Electrode drift was checked before and after the survey and was found to be negligible (Petiau electrodes are known to be stable). It exhibits a strong (80 mV) anomaly and negative anomalies (−20 to −40 mV). The positions of an area with the ground being wet (Zone A) and the spring (Zone B) are also identified on Fig. 10(b). Zone A is consistent with the positive anomaly while Zone B is consistent with the end of one of the negative self-potential anomalies.

3.3. Petrophysical measurements

In water-saturated conditions with acidic pore waters, the alteration of granites involves the transformation of primary minerals (mica and alkali feldspars) into secondary clay minerals especially kaolinite $Al_4(OH)_8[Si_4O_{10}]$. For instance, the alteration of orthoclase ($K[AlSi_3O_8]$, a potassium feldspar) and albite ($Na[AlSi_3O_8]$, a plagioclase) yield (see Stoch & Sikora 1976; Yatsu 1988; Wilson 2004; Nguetnkam *et al.* 2008)

$$4Me\,[AlSi_3O_8] + 4H_2O + 2CO_2 \Leftrightarrow Al_4(OH)_8\,[Si_4O_{10}] + 2MeCO_3 + 8SiO_2, \quad (12)$$

where Me = K and Na. Usually, the alteration path involves the slow dissolution of alkali feldspars and plagioclase (with a typical timescale of ∼100 000 yr) and the precipitation of kaolinite (see Blum 1994). Schiavon (2007) demonstrated that granite weathering and

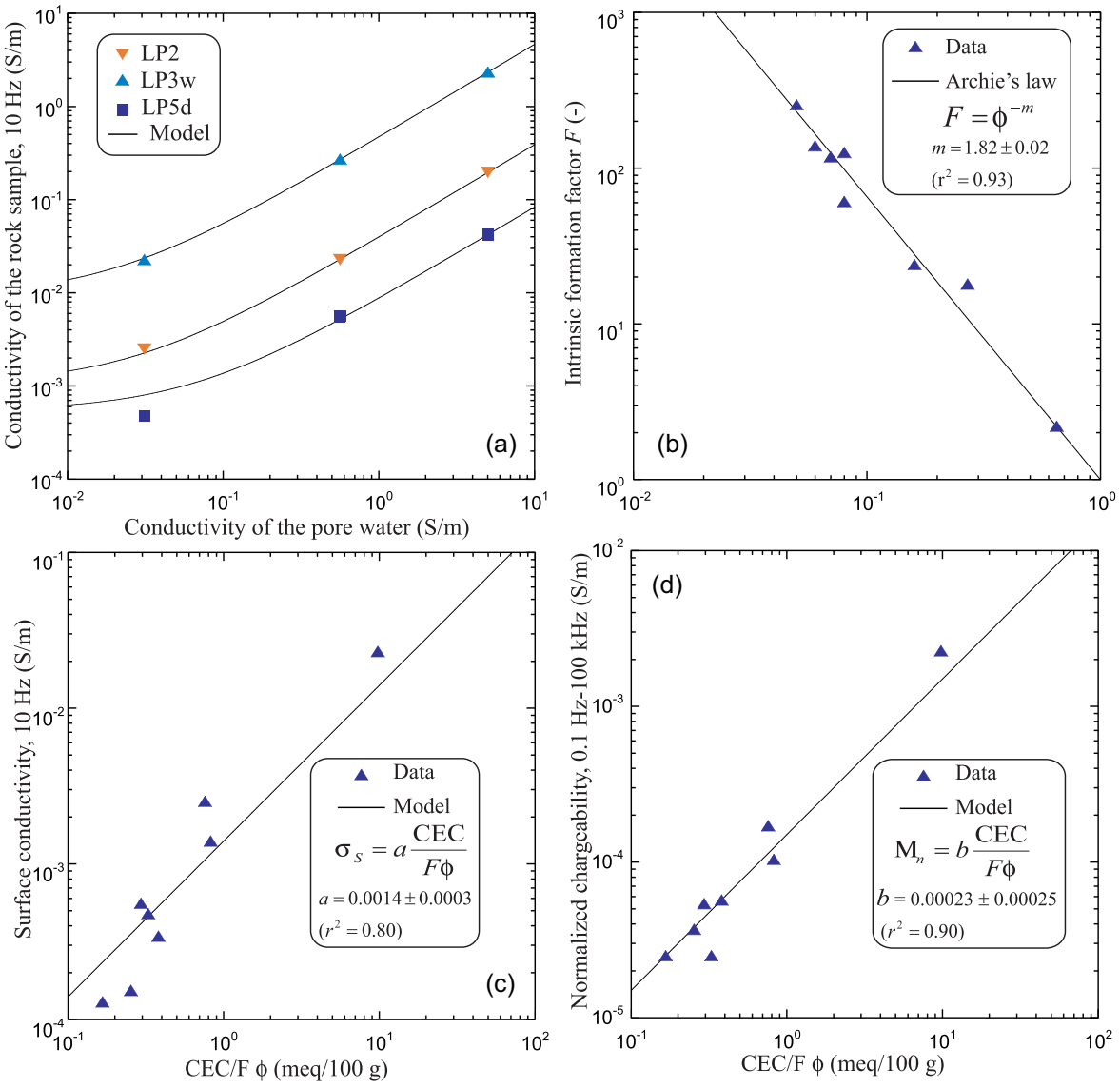

Figure 16. Petrophysical analysis of the electrical properties of the core samples. (a) Relationship between the conductivity of the rock versus the conductivity of the pore water (NaCl, 25 °C). The data are fitted for each core sample to get the formation factor and the surface conductivity. (b) Formation factor versus porosity and fit with Archie's law. The fit is used to get the value of the porosity exponent m. (c) Relationship between the surface conductivity and the CEC divided by the bulk tortuosity of the pore space. (d) Relationship between the normalized chargeability and the CEC divided by the bulk tortuosity of the pore space.

the formation of authigenic kaolinite can take place in urban environments at a much faster rates (decades), especially in presence of SO_2 in acidic conditions. Kaolinization takes place in hydrothermal conditions such as for the quartz monzonite of Mount Princeton (Colorado, see Richards *et al.* 2010). A weathering classification standard for granite has been developed by Woo *et al.* (2006) and weathering and alteration can be connected to seismic velocities (Woo *et al.* 2006; Lin *et al.* 2014, 2021).

In order to test the effect of porosity and alteration (through CEC, measurements) on the complex conductivity of granite, we collected eight samples from the test site. The samples were collected downstream the Lampy dam from outcrops. There are weathered and altered core samples. The core samples are shown in Fig. 12. They were first washed, dried and then saturated under vacuum with a NaCl solution at 0.032 S m^{-1} (25 °C) for the first set of complex conductivity measurements. Two other high salinities (conductivities at 0.56 and 5.0 S m^{-1} at 5 °C) were used to obtain a complete data set to get in turn the formation factor and the surface conductivity. The change of salinity was done by diffusion in the brine of higher salinity.

The porosity was obtained from weight and volume measurements, while the CEC was measured using the cobalthexamine method (see Table 1). The in-phase and quadrature conductivity spectra are shown in Fig. 13. As expected, the in-phase conductivity increases slightly with the frequency, while the quadrature conductivity shown a plateau at low frequencies corresponding to the induced polarization effect and an increase of its amplitude with frequency at higher frequencies. The second mechanism (dominant

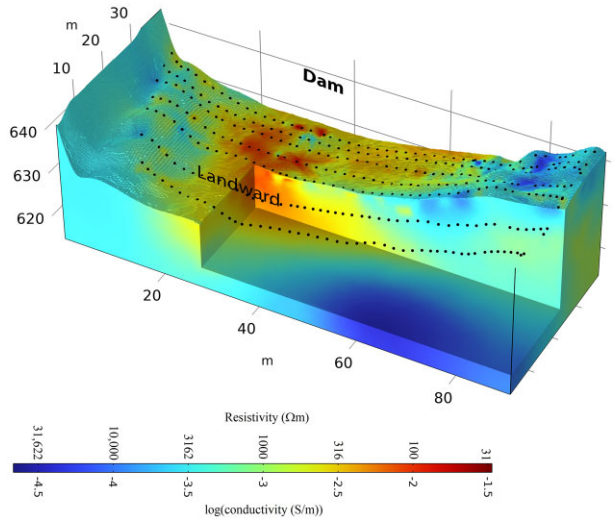

Figure 17. 3-D electrical resistivity/electrical conductivity tomogram of the ground downstream the dam. The black dots correspond to the position of the electrodes. The forward modelling is done with 34 992 tetrahedral elements. The element sizes within the model space range from a maximum of 4 m to a minimum of 2 m with a curvature factor of 0.3 m. In the vicinity of the electrodes, the mesh is refined with element sizes varying between 0.8 and 0.03 m and a curvature factor of 0.2 m.

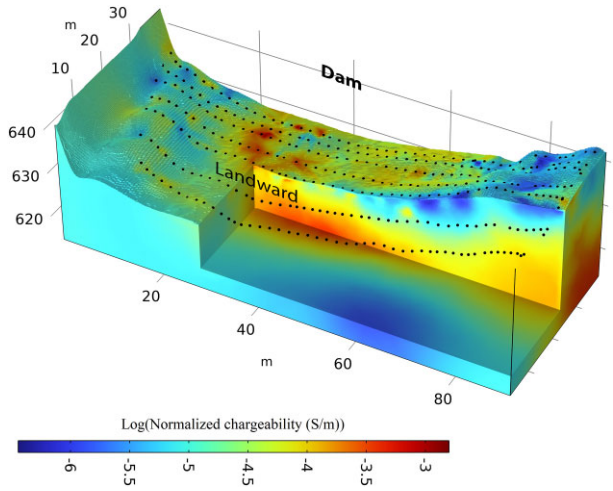

Figure 18. 3-D normalized chargeability tomogram of the ground downstream the dam. The black dots correspond to the position of the electrodes. The normalized chargeability varies over three orders of magnitude. The normalized chargeability is controlled by both the water content and the CEC of the granite. The same finite-element approach with 34 992 tetrahedral elements is used.

at high frequencies) is known as the Maxwell–Wagner polarization mechanism.

Fig. 14 shows the normalized chargeability versus the low salinity conductivity, which corresponds here to the surface conductivity (which can be independently obtained when the conductivity of the rock samples is plotted versus the pore water). The slope is predicted to be equal to $R = 0.10$, which is the case. Fig. 15 shows that the polarization can be either characterized by the low-frequency quadrature conductivity or the normalized chargeability obtained from the dispersion of the in-phase conductivity with the frequency. The results are consistent with the work done by Zhang *et al.* (2023) for volcanic rocks (compare Figs 15a and b).

Fig. 16(a) shows the results the in-phase conductivity data of the rock samples versus the pore water conductivity. The data are fitted with a linear conductivity model and the slope used to determine the formation factor. The data are also used to determine the value of the surface conductivity. In Fig. 16(b), the formation factors are reported versus the corresponding porosities and the data are fitted with Archie's law with a porosity exponent $m = 1.82$. In Figs 16(c) and (d), the surface conductivity and normalized chargeability are reported as a function of the CEC divided by the bulk tortuosity of the pore space (corresponding to the product of the formation factor and connected porosity). The data for the granite core samples are consistent with the petrophysical model described above.

4. TOMOGRAMS AND INTERPRETATIONS

4.1. Induced polarization

The resistivity and normalized chargeability tomograms are shown in Figs 17 and 18. The conductivity is in the range $10^{-1.5}$ to $10^{-4.5}$ S m^{-1}, while the normalized chargeability is in the range 10^{-3} to 10^{-6} S m^{-1}. The convergence in the inversion of the observed data is good as shown in Fig. 19 with low data RMS (root mean square) errors in both cases.

The conductivity and normalized chargeability tomograms are jointly interpreted with the petrophysical model described in Section 2 (eqs 5 and 6) in terms of water content and CEC tomograms (Figs 20 and 21). The alteration of granite produced kaolinite (Nguetnkam *et al.* 2008) and the CEC of kaolinite is typically in the range 3–15 meq per 100 g (Ma & Eggleton 1999) consistent with the upper bound found in the tomogram shown in Fig. 21. Then the water content and CEC tomograms are combined to provide an image of the permeability distribution using eq. (7).

The permeability tomogram is shown in Fig. 22. The values are comprised between 10^{-8} m^2 for the high-permeability conduit to 10^{-18} m^2 for what should be called an aquitard. The area characterized by high permeability values and high water contents in the form of a conduit is consistent with an area where the soil is characterized by a high degree of moisture (see Zone A in Fig. 10b). The area just above the low-permeability horizontal structure is known to channel shallow groundwater flow in a perched aquifer toward the spring (Zone B in Fig. 10b).

In Fig. 23, we plot the normalized chargeability versus the conductivity. When the data points are close to the line corresponding to a slope with $R = 0.10$, this means that surface conductivity (due to clay minerals) dominates the conductivity response of the material. This is the case for the data corresponding to the high normalized chargeability and conductivity values, which corresponds to altered granites likely associated with the process of kaolinization of pristine granites. The other domain characterized by low normalized chargeability and conductivity values corresponds to fresh (unaltered granites). For granite with open cracks, the conductivity is expected to be dominated by the bulk conductivity component and the water content rather than by the CEC.

4.2. Self-potential

Using the permeability distribution (Fig. 22) and the boundary conditions for the investigated block (Fig. 24), we built a preliminary groundwater flow model shown in Fig. 25. The partial differential equations are solved with Comsol Multiphysics. The boundary

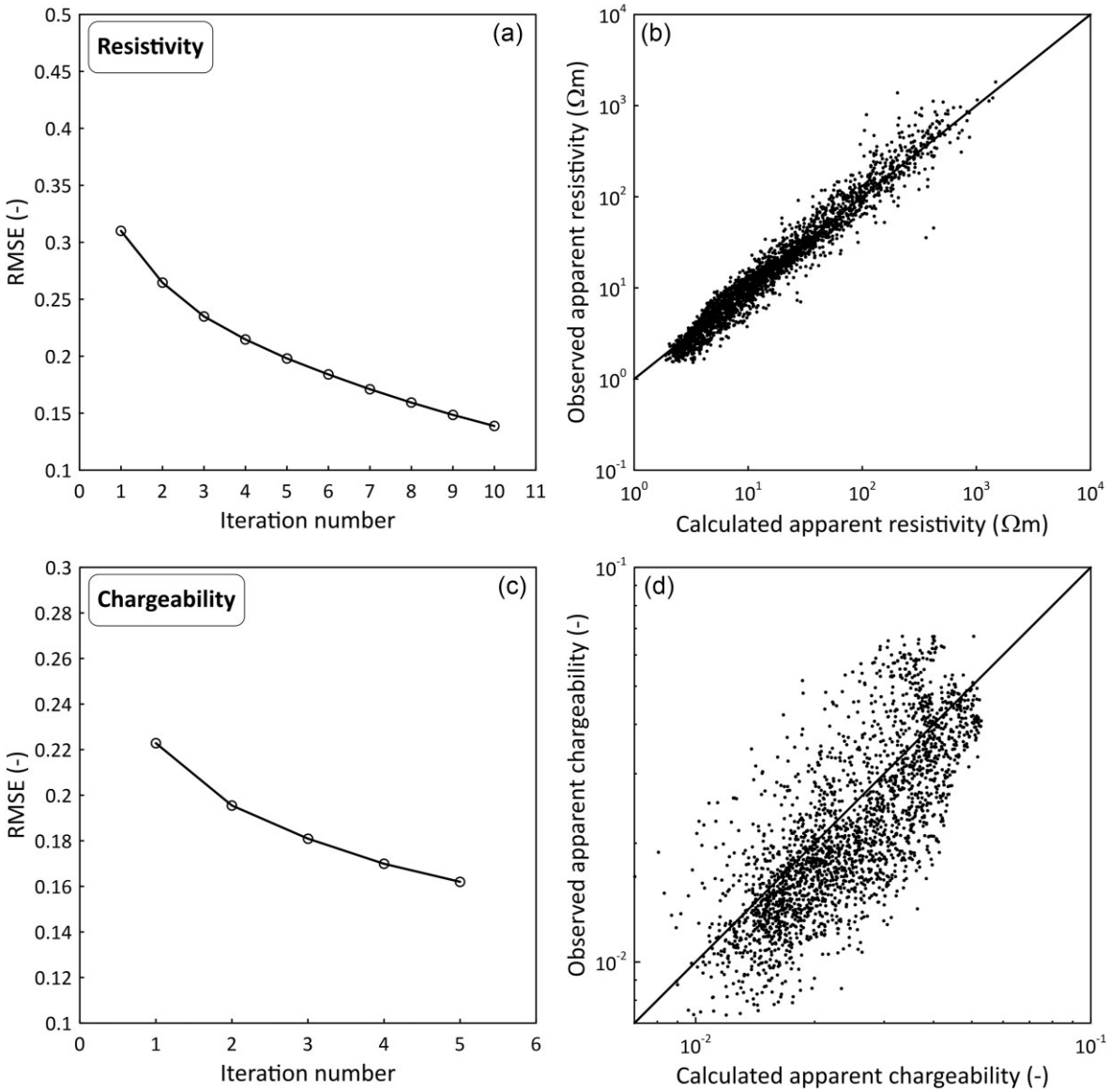

Figure 19. Convergence of the inversion algorithm. (a) Convergence of the data misfit during the iteration of the inversion process of the apparent resistivity data. RMSE denotes the root mean square error for the apparent resistivity data. (b) Comparison between the observed apparent resistivity and the calculated apparent resistivity at the last iteration. from the resistivity tomogram obtained. (c) Convergence of the data misfit during the iteration of the inversion process of the apparent chargeability data. RMSE denotes the root mean square error for the apparent chargeability data. (d) Comparison between the observed apparent chargeabilities and the calculated apparent chargeabilities from the chargeability tomogram obtained at the last iteration.

conditions are (i) pressure condition at the bottom boundary, (ii) no flow on the sides (we do not attempt to model the leakage and flow in the unconfined aquifer above the aquitard) and (iii) open flow boundary at the ground surface (atmospheric boundary condition at the ground surface).

Then, we used this groundwater flow model to build a prior source current density model for the self-potential problem using the Darcy velocity and the relationship between the excess charge density and the permeability (see Appendix B). We update this source current density model into a posterior source current density model that is consistent with the self-potential data using also in the inverse problem the electrical conductivity distribution obtained thanks to the induced polarization survey (see Appendix B for details and Fig. 26 for the optimization of the regularization parameter λ). Finally, this source current density is converted into a groundwater flow model using the permeability distribution for the effective charge density $\mathbf{u} = \mathbf{j}_S/\hat{Q}_V(k)$. The optimization of the regulation parameter is done with the L-curve approach (Fig. 26). The prior and posterior current density distributions are shown in Fig. 27. The final groundwater flow model is shown in Fig. 28(a). To achieve this result, we use the the flow chart shown in Fig. 6.

We can finally discuss the updated groundwater flow model in terms of the two flow anomalies discussed in Section 3 of the paper (Zones A and B in Fig. 10b). The wet area (Zone A) is explained by a focused groundwater flow likely passing below the dam into the granite. This anomaly is similar to the anomalies observed in

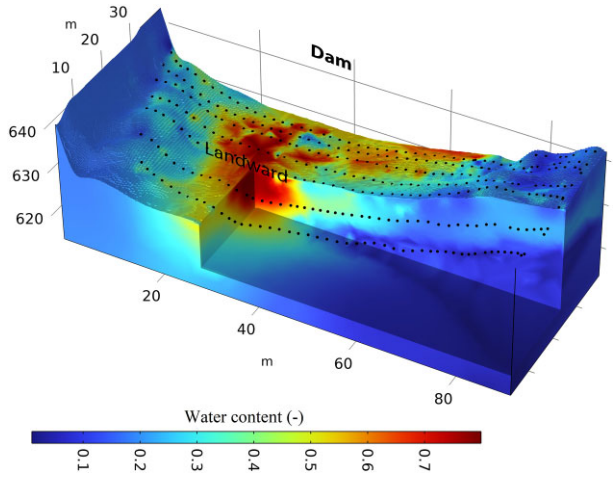

Figure 20. Tomogram of the (volumetric fraction) water content θ obtained by combining the electrical conductivity and normalized chargeability tomograms. The area of high water content is probably fractured.

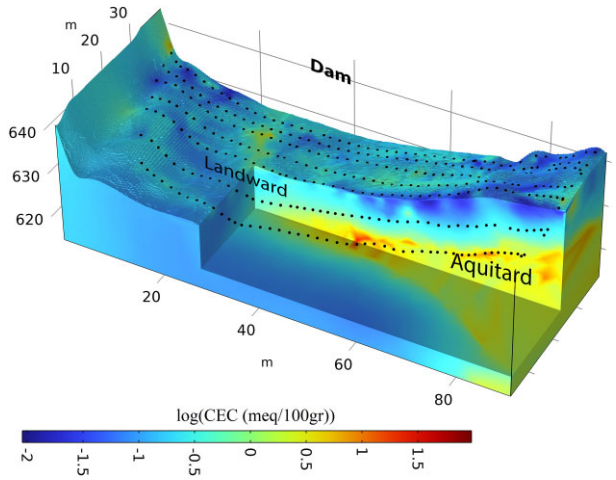

Figure 21. Tomogram of the CEC obtained by combining the electrical conductivity and normalized chargeability tomograms. Low values of the CEC < 1 meq per 100 g would correspond to poorly altered granite, while values comprised between 1 to 30 meq per 100 g would corresponds to altered granites (generally with a high content of kaolinite).

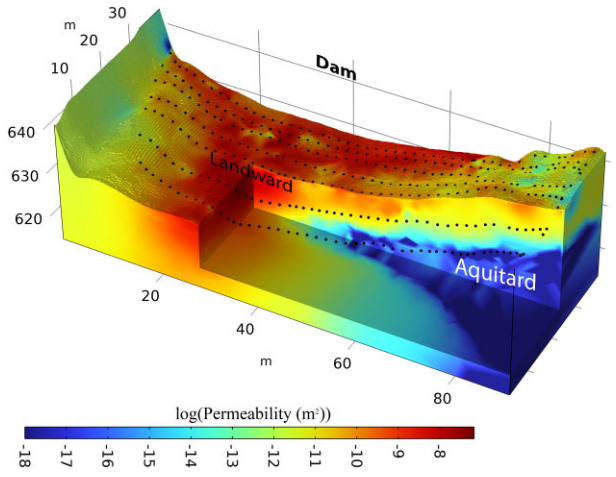

Figure 22. Tomogram of the permeability obtained by combining the electrical conductivity and normalized chargeability tomograms. We can see on the right-hand side of the tomogram a low permeability domain (10^{-15} to 10^{-18} m^2) corresponding to an aquitard probably underlying a perched aquifer. We can also observe a high permeability conduit with permeability higher than 1 Darcy ($\sim 10^{-12}$ m^2) corresponding likely to a fractured area.

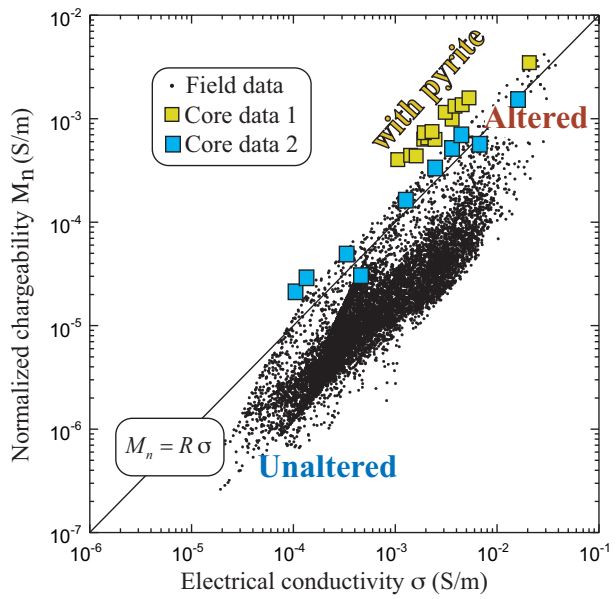

Figure 23. Normalized chargeability versus electrical conductivity. Comparison between laboratory data and field data for granites. High normalized chargeability values characterized altered granites, while low normalized chargeability values correspond to granites. The core data set 1 is from Britany (France) and contains pyrite, while the Core data set 2 is from the field site (M_n determined between 0.1 Hz and 1 kHz and in phase conductivity evaluated at 33 Hz, pore water conductivity of 0.1 S m^{-1} at 25 °C). The plain line is obtained when surface conductivity dominates the bulk conductivity in the in-phase conductivity equation.

geothermal areas and associated with the upwelling of hot ground water in fault zones (see for instance Revil & Pezard 1998; Jardani & Revil 2009).

The occurrence of the spring (Zone B) is explained by water coming from the side of the dam in the formed of a perched aquifer with water flowing above the kaolinite-rich aquitard that is imaged in the permeability tomogram. The source of this flow may originate from the channel C4 shown in Fig. 28(b). This type of anomaly is similar in essence to the negative self-potential anomaly associated with groundwater flow in a palaeochannel of the Rhône River by Revil *et al.* (2005a). This confirms the analysis of the monitoring system data, which did not show any singular behaviour since the spring (Zone B) appeared. This result is comforting about the dam's safety because it shows that there is no direct flow between the reservoir and the toe of the dam.

This works illustrates a powerful combination of the self-potential and induced polarization geophysical methods used in concert to produce a groundwater flow distribution that is hydro-geologically meaningful.

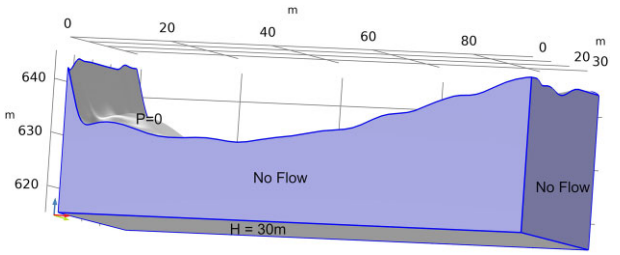

Figure 24. Ground water flow conditions for the simulations. The flow model is very simple. We assume no flow boundaries on the side of the block and a difference of pressure between the lower and the upper boundary conditions (atmospheric pressure). The porosity and permeability distributions are those determined from the geoelectrical methods. The ground water flow is modelled with the finite-element technique using 40 744 tetrahedral elements.

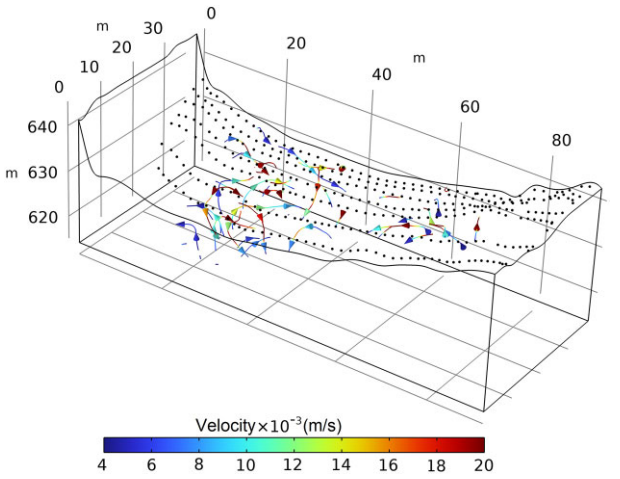

Figure 25. Prior groundwater flow model determined from the permeability model and the boundary conditions for the groundwater flow. The figure shows the distribution of the Darcy velocity greater than 4×10^{-3} m s^{-1}. It shows an area of focused flow consistent with the localization of the moisture anomaly A in Fig. 10(b).

5. CONCLUSIONS

We have proposed a new scheme to combine a 3-D induced polarization survey with a self-potential map to get a 3-D image of groundwater flow that is physically meaningful in terms of pattern and boundary conditions. The proposed methodology is applied to the dam of Lampy, one of the oldest dams in France, to investigate groundwater pattern downstream of this dam. The substratum is made of granite with different degrees of alteration. Two areas are observed in the permeability tomogram resulting from the induced polarization survey. First, a vertical permeability conduit below an area where the soil is observed to be wet can be observed/inferred from the geophysical survey. In addition, a shallow aquitard is observed in the granite below the position of the Spring B. Shallow groundwater flow above this perched aquifer is able to explain the presence of the spring at the bottom of the dam. The approach developed in the present paper is very general and could represent a welcome step in hydrogeophysics to image non-intrusively groundwater flow in the critical zone of the Earth. Further works will be

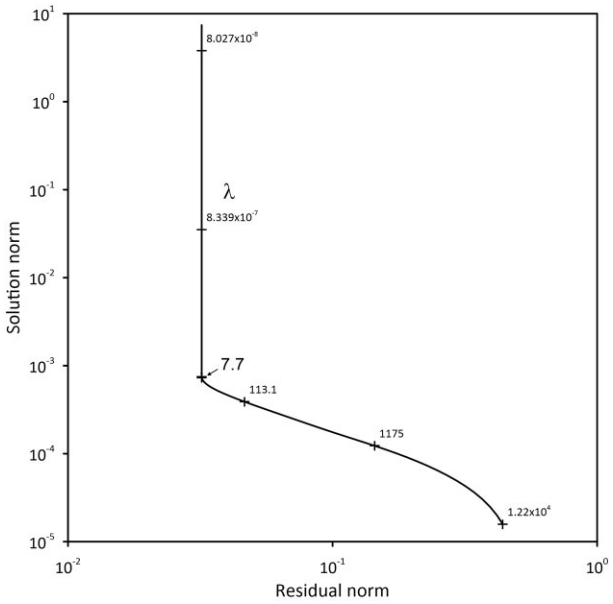

Figure 26. *L*-curve for the inversion of the self-potential data. The trade-off (regularization) parameter λ is determined at the corner of the *L*-curve with an optimized value of 7.7 (the values provided in the figure are different values of the trade-off parameters λ). The standard deviation used for the measurement is equal to 5 mV.

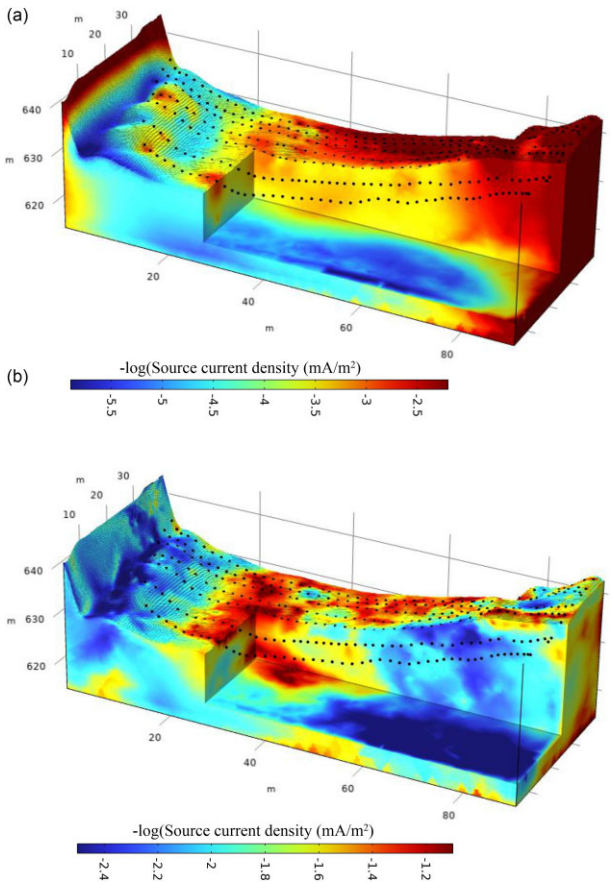

Figure 27. Streaming current density source distribution. (a) Prior source current density distribution determined from the permeability distribution and groundwater flow boundary conditions. (b) Posterior source current density distribution determined from the prior source current distribution and the information contained in the self-potential map distribution measured at the ground surface. The forward modelling is based on the finite-element approach. It uses 33 627 tetrahedral elements.

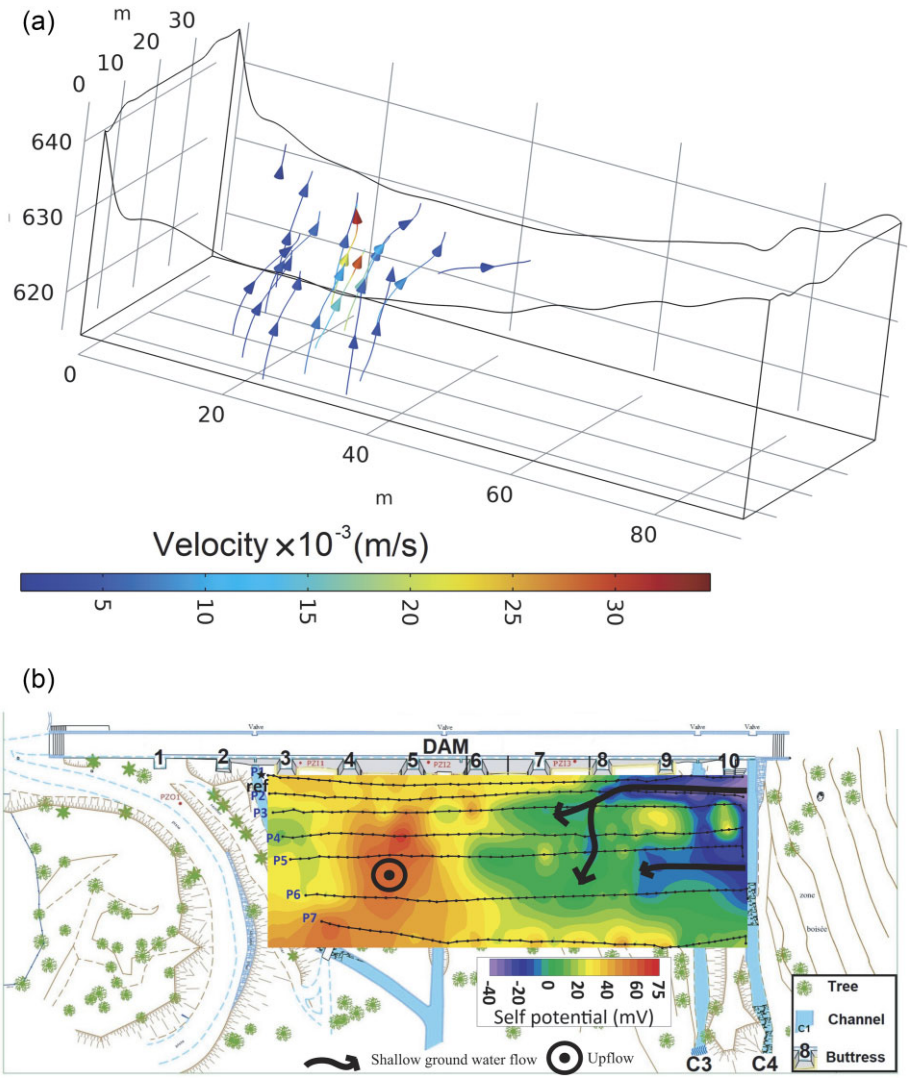

Figure 28. Flow directions. (a) Groundwater flow model in terms of streamlines in the investigated area (threshold of the Darcy velocity 2×10^{-3} m s^{-1}). The area of upwelling of the ground water is in agreement with the wet soil area (Zone A in Fig. 7b). (b) Reconstructed self-potential map from the updated groundwater flow model shown in Fig. 19(a). The self-potential map is completely reconstructed with a correlation coefficient $R^2 = 0.999$ (root mean square RMS, error: 2×10^{-2} mV).

dedicated to a better evaluation of the limits if the methods using synthetic cases as well as looking at the uncertainty analysis as well as extending the approach to anisotropic formations.

ACKNOWLEDGMENTS

This work was able to be carried out thanks to the results of the ALCOTRA project RITA funded by the European Community. We thank VNF for access to the site. We thank the three referees and the editors for the fruitful reviews that have help to shape a much better version of our manuscript. We thank Scott Ikard for an earlier review of our paper. This paper is dedicated to Abderrahim Jardani for the tremendous achievements he performed in the field of hydrogeophysics.

DATA AVAILABILITY

The data used in thIS paper could be obtained through a request to the corresponding author after an embargo of two years.

REFERENCES

Abdulsamad, F., Chitimbo, T., Revil, A., Prime, N. & Plé, O., 2023, Imaging the water content of rammed earth materials with induced polarization, *Eng. Geol.,* **322,** 107182. https://doi.org/10.1016/j.enggeo.2023.107182.

Abdulsamad, F., Revil, A., Soueid Ahmed, A., Coperey, A., Karaoulis, M., Nicaise, S. & Peyras, L., 2019. Induced polarization tomography applied to the detection and the monitoring of leaks in embankments dams and dikes, *Eng. Geol.,* **254,** 89–101. https://doi.org/10.1016/j.enggeo.2019.04.001.

Ahmad, M.U., 1969. A laboratory study of streaming potentials, *Geophys. Prospect.,* **12**(1), 49–64. https://doi.org/10.1111/j.1365-2478.1964.tb01889.x.

Archie, G.E., 1942. The electrical resistivity log as an aid in determining some reservoir characteristics, *Pet. Trans. AIME,* **146,** 54–62. https://doi.org/10.2118/942054-G.

Binley, A., Hubbard, S.S., Huisman, J.A., Revil, A., Robinson, D.A., Singha, K. & Slater, L.D., 2015. The emergence of hydrogeophysics for improved understanding of subsurface processes over multiple scales, *Water Resour. Res.,* **51,** 3837–3866, https://doi.org/10.1002/2015WR017016.

Blum, A.E., 1994. Feldspars in weathering, In: Parsons, I (eds) *Feldspars and Their Reactions*. Kluwer, The Netherlandspp. 595–630,

Series 421. Springer, Dordrecht. https://doi.org/10.1007/978-94-011-1106-5_15.

Bolève, A., Crespy, A., Revil, A., Janod, F. & Mattiuzzo, J.L., 2007b. Streaming potentials of granular media: influence of the Dukhin and Reynolds numbers, *J. geophys. Res.: Solid Earth,* **112**(B8), https://doi.org/10.1029/2006JB004673.

Bolève, A., Revil, A., Janod, F., Mattiuzzo, J.L. & Jardani, A., 2007a. Forward modeling and validation of a new formulation to compute self-potential signals associated with ground water flow, *Hydrol. Earth Syst. Sci.,* **11**(5), 1661–1671. https://doi.org/10.5194/hess-11-1661-2007.

Börner, F.D., Gruhne, M. & Schön, J.H., 1993. Contamination indications derived from electrical properties in the low frequency range, *Geophys. Prospect.,* **41,** 83–98. https://doi.org/10.1111/j.1365-2478.1993.tb00566.x.

Bremer, M., Kulenkampff, J. & Schopper, J.R., 1992. An attempt of deterministic interpretation of KTB-Oberpfalz-VB standard logs, *Sci. Drill.,* **3,** 6–15.

Casagrande, L., 1983. Stabilization of soils by means of electro-osmosis: state of the art, *J. Boston Soc. Civil Eng.,* **69**(2), 255–302.

Castermant, J., Mendonça, C.A., Revil, A., Trolard, F., Bourrié, G. & Linde, N., 2008. Redox potential distribution inferred from self-potential measurements associated with the corrosion of a burden metallic body, *Geophys. Prospect.,* **56,** 269–282, https://doi.org/10.1111/j.1365-2478.2007.00675.x.

Delville, A., 1991. Modeling the clay-water interface, *Langmuir,* **7**(3), 547–555, https://doi.org/10.1021/la00051a022.

Fransisco, J.M., Fernando, D., Jesús, G., Wenceslao, M., Manuel, L. & Lourdes, G., 2018. Identification of leakage and potential areas for internal erosion combining ERT and IP techniques at the Negratín Dam left abutment (Granada, southern Spain), *Eng. Geol.,* **240,** 74–80. https://doi.org/10.1016/j.enggeo.2018.04.012.

Friborg, J., 1996. *Experimental and Theoretical Investigations into the Streaming Potential Phenomenon with Special Reference to Applications in Glaciated Terrain,* Ph.D. thesis, Lulea University of Technology, Sweden.

Ghorbani, A., Chitimbo, T., Revil, A., Prime, N., Zhang, K., Fu, T. & Plé, O., 2023. Water content imaging during capillary rise within a rammed earth structure, *Eng. Geol.,* **325,** 107305. https://doi.org/10.1016/j.enggeo.2023.107305.

Gouy, G.L., 1910. Sur la constitution de la charge électrique à la surface d'un électrolyte, *J. Phys. Théor. Appl.,* **9,** 457–468. https://doi.org/10.1051/jphystap:019100090045700.

Grech, R. *et al.* 2008. Review on solving the inverse problem in EEG source analysis, *J. NeuroEng. Rehab,* **5**(25), 1–33. http://dx.doi.org/10.1186/1743-0003-5-25.

Hansen, P.C., 1998. Rank-deficient and discrete ill-posed problems, in *Numerical Aspects of Linear Inversion,* 247 pp., Society for Industrial and Applied Mathematics, SIAM, MM04, Philadelphia, PA.

Hao, N., Moysey, S.M.J., Powell, B.A. & Ntarlagiannis, D., 2016. Comparison of the surface ion density of silica gel evaluated via spectral induced polarization versus acid–base titration, *J. appl. Geophys.,* **135,** 427–435. https://doi.org/10.1016/j.jappgeo.2016.01.014.

Himi, M., Casado, I., Sendros, A., Lovera, R., Rivero, L. & Casas, A., 2018. Assessing preferential seepage and monitoring mortar injection through an earthen dam settled over a gypsiferous substrate using combined geophysical methods, *Eng. Geol.,* **246,** 212–221. https://doi.org/10.1016/j.enggeo.2018.10.002.

Ishido, T. & Mizutani, H., 1981. Experimental and theoretical basis of electrokinetic phenomena in rock-water systems and its applications to geophysics, *J. geophys. Res.,* **86**(NB3), 1763–1775. https://doi.org/10.1029/JB086iB03p01763.

Jardani, A. & Revil, A., 2009. Stochastic joint inversion of temperature and self-potential data, *Geophys. J. Int.,* **179**(1), 640–654. https://doi.org/10.1111/j.1365-246X.2009.04295.x.

Jardani, A., Revil, A., Bolève, A. & Dupont, J.P., 2008. Three-dimensional inversion of self-potential data used to constrain the pattern of groundwater flow in geothermal fields, *J. geophys. Res.,* **113,** B09204, https://doi.org/10.1029/2007JB005302.

Jardani, A., Revil, A., Bolève, A., Dupont, J.P., Barrash, W. & Malama, B., 2007. Tomography of the Darcy velocity from self-potential measurements, *Geophys. Res. Lett.,* **34,** L24403, https://doi.org/10.1029/2007GL031907.

Jardani, A., Revil, A., Slob, E. & Söllner, W., 2010. Stochastic joint inversion of 2D seismic and seismoelectric signals in linear poroelastic materials, *Geophysics,* **75**(1), N19–N31. https://doi.org/10.1190/1.3279833.

Johnson, T.C., Versteeg, R.J., Ward, A., Day-Lewis, F.D. & Revil, A., 2010. Improved hydrogeophysical characterization and monitoring through parallel modeling and inversion of time-domain resistivity and induced-polarization data, *Geophysics,* **75,** WA27–WA41. https://doi.org/10.1190/1.3475513.

Jougnot, D., Linde, N., Revil, A. & Doussan, C., 2012. Derivation of soil-specific streaming potential electrical parameters from hydrodynamic characteristics of partially saturated soils, *Vadoze Zone J.,* **11**(1), https://doi.org/10.2136/vzj2011.0086.

Karaoulis, M., Revil, A., Werkema, D.D., Minsley, B., Woodruff, W.F. & Kemna, A., 2011. Time-lapse 3D inversion of complex conductivity data using an active time constrained (ATC) approach, *Geophys. J. Int.,* **187,** 237–251, https://doi.org/10.1111/j.1365-246X.2011.05156.x.

Kemna, A. *et al.*, 2012. An overview of the spectral induced polarization method for near-surface applications, *Near Surf. Geophys.,* **10,** 453–468. https://doi.org/10.3997/1873-0604.2012027.

Kuwano, O., Yoshida, S., Nakatani, M. & Uyeshima, M., 2015. Origin of transient self-potential signals associated with very long period seismic pulses observed during the 2000 activity of Miyakejima volcano, *J. geophys. Res.—Solid Earth,* **120,** 3544–3565. https://doi.org/10.1002/2014JB011740.

Leroy, P., Jougnot, D., Revil, A., Lassin, A. & Azaroual, M., 2012. A double layer model of the gas bubble/water interface, *J. Colloid Interface Sci.,* **388**(1), 243–256, https://doi.org/10.1016/j.jcis.2012.07.029.

Leroy, P. & Revil, A., 2004. A triple layer model of the surface electrochemical properties of clay minerals, *J. Colloid Interface Sci.,* **270**(2), 371–380. https://doi.org/10.1016/j.jcis.2003.08.007.

Leroy, P., Revil, A., Kemna, A., Cosenza, P. & Ghorbani, A., 2008. Complex conductivity of water-saturated packs of glass beads, *J. Colloid Interface Sci.,* **321**(1), 103–117. https://doi.org/10.1016/j.jcis.2007.12.031.

Lin, D. *et al.* 2021. Disturbed granite identification by integrating rock mass geophysical properties, *Int. J. Rock Mech. Min. Sci.,* **138,** 104596, https://doi.org/10.1016/j.ijrmms.2020.104596.

Lin, D., Sun, Y., Zhang, W., Yuan, R., He, W., Wang, B. & Shang, Y., 2014. Modifications to the GSI for granite in drilling, *Bull. Eng. Geol. Environ.,* **73**(4), 1245–1258. https://doi.org/10.1007/s10064-014-0581-0.

Linde, N. & Revil, A., 2007. Inverting self-potential data for redox potentials of contaminant plumes, *Geophys. Res. Lett.,* **34,** L14302, https://10.1029/2007GL030084.

Ling, C., Revil, A., Qi, Y., Abdulsamad, F., Shi, P., Nicaise, S. & Peyras, L., 2019. Application of the Mise-à-la-Masse method to detect the bottom leakage of water reservoirs, *Eng. Geol.,* **261,** 105272, https://doi.org/10.1016/j.enggeo.2019.105272.

Ma, C. & Eggleton, R.A., 1999. The CEC of kaolinite, *Clays Clay Miner.,* **47**(2), 174–180. https://doi.org/10.1346/CCMN.1999.0470207.

Maineult, A., Bernabé, Y. & Ackerer, P., 2006. Detection of advected, reacting redox fronts from self-potential measurements, *J. Contam. Hydrol.,* **86**(1-2), 32–52. https://doi.org/10.1016/j.jconhyd.2006.02.007.

Mao, D., Revil, A. & Hinton, J., 2016. Induced polarization response of porous media with metallic particles.—Part 4. Detection of metallic and nonmetallic targets in time-domain-induced polarization tomography, *Geophysics,* **81**(4), D359–D375, https://doi.org/10.1190/GEO2015-0480.1.

Merlet, I. & Gotman, J., 2001. Dipole modeling of scalp electroencephalogram epileptic discharges: correlation with intracerebral fields, *Clin. Neurophysiol.,* **112,** 414–430, https://doi.org/10.1016/S1388-2457(01)00458-8.

Nguetnkam, P., Kamga, R., Villiéras, F., Ekodeck, G.E. & Yvon, J., 2008. Variable weathering response of granite in tropical zones. Example of two sequences studied in Cameroon (Central Africa), *C.R. Geosci.,* **340**(7), 451–461. https://doi.org/10.1016/j.crte.2008.02.002.

Niu, Q., Revil, A. & Saidian, M., 2016. Salinity dependence of the complex surface conductivity of the Portland sandstone, *Geophysics,* **81**(2), D125–D140. https://doi.org/10.1190/GEO2015-0426.1.

Panthulu, T.V., Krishnaiah, C. & Shirke, J.M., 2001. Detection of seepage paths in earth dams using self-potential and electrical resistivity methods, *Eng. Geol.,* **59,** 281–295. https://doi.org/10.1016/S0013-7952(00)00082-X.

Pengra, D., Li, S.X. & Wong, P., 1999. Determination of rock properties by low-frequency AC electrokinetics, *J. geophys. Res.,* **104,** 485–508. https://doi.org/10.1029/1999JB900277.

Revil, A., 1999. Ionic diffusivity, electrical conductivity, membrane and thermoelectric potentials in colloids and granular porous media: a unified model, *J. Colloid Interface Sci.,* **212,** 503–522. https://doi.org/10.1006/jcis.1998.6077.

Revil, A., 2013a. On charge accumulation in heterogeneous porous rocks under the influence of an external electric field, *Geophysics,* **78**(4), D271–291. https://doi.org/10.1190/geo2012-0503.1.

Revil, A., 2013b. Effective conductivity and permittivity of unsaturated porous materials in the frequency range 1mHz-1 GHz, *Water Resour. Res.,* **49,** 306–327. https://doi.org/10.1029/2012WR012700.

Revil, A., Cary, L., Fan, Q., Finizola, A. & Trolard, F., 2005a. Self-potential signals associated with preferential groundwater flow pathways in a buried paleo-channel, *Geophys. Res. Lett.,* **32,** L07401, https://doi.org/10.1029/2004GL022124.

Revil, A., Ehouarne, L. & Thyreault, E., 2001. Tomography of self-potential anomalies of electrochemical nature, *Geophys. Res. Lett.,* **28**(23), 4363–4366. https://doi.org/10.1029/2001GL013631.

Revil, A., Ghorbani, A., Jougnot, D., Yven, B., Grgic, D., Bretaudeau, F. & Deparis, J., 2023b. Induced polarization of clay-rich materials. Part 2. The effect of anisotropy, *Geophysics,* **88**(6), https://doi.org/10.1190/geo2022-0511.1.

Revil, A. & Gresse, M., 2021. Induced polarization as a tool to assess alteration in volcanic areas: a review, *Minerals,* **11,** 962, https://doi.org/10.3390/min11090962.

Revil, A. & Jardani, A., 2013. *The Self-potential Method: Theory and Applications in Environmental Geosciences*. Cambridge University Press.

Revil, A., Karaoulis, M., Johnson, T. & Kemna, A., 2012. Review: some low-frequency electrical methods for subsurface characterization and monitoring in hydrogeology, *Hydrol. J.,* **20**(4), 617–658. https://doi.org/10.1007/s10040-011-0819-x.

Revil, A., Leroy, P. & Titov, K., 2005b. Characterization of transport properties of argillaceous sediments. Application to the Callovo-oxfordian argillite, *J. Geophys. Res.,* **110,** B06202. https://doi.org/10.1029/2004JB003442.

Revil, A., Linde, N., Cerepi, A., Jougnot, D., Matthäi, S. & Finsterle, S., 2007. Electrokinetic coupling in unsaturated porous media, *J. Colloid Interface Sci.,* **313**(1), 315–327. https://doi.org/10.1016/j.jcis.2007.03.037.

Revil, A. & Pezard, P.A., 1998. Streaming electrical potential anomaly along faults in geothermal areas, *Geophys. Res. Lett.,* **25**(16), 3197–3200. https://doi.org/10.1029/98GL02384.

Revil, A., Qi, Y., Ghorbani, A., Gresse, M. & Thomas, D.M., 2021. Induced polarization of volcanic rocks. 5. Imaging the temperature field of shield volcanoes, *Geophys. J. Int.,* **225,** 1492–1509. https://doi.org/10.1093/gji/ggab039.

Revil, A., Soueid Ahmed, A. & Jardani, A., 2017. Self-potential: a non-intrusive groundwater flow sensor, *J. Environ. Eng. Geophys.,* **22**(3), 235–247. https://doi.org/10.2113/JEEG22.3.235.

Revil, A., Su, Z., Zhu, Z. & Maineult, A., 2023a. Self-potential as a tool to monitor redox reactions at an ore body: a sandbox experiment, *Minerals,* **13**(6) 716. https://doi.org/10.3390/min13060716.

Richards, K., Revil, A., Jardani, A., Henderson, F., Batzle, M. & Haas, A., 2010. Pattern of shallow ground water flow at Mount Princeton Hot Springs, Colorado, using geoelectrical methods, *J. Volc. Geotherm. Res.,* **198,** 217–232. https://doi.org/10.1016/J.JVOLGEORES.2010.09.001.

Rittgers, J.B., Revil, A., Planès, T., Mooney, M.A. & Koelewijn, A.R., 2015. 4D imaging of seepage in earthen embankments with time-lapse inversion of self-potential data constrained by acoustic emissions localization, *Geophys. J. Int.,* **200,** 758–772. https://doi.org/10.1093/gji/ggu432.

Rosen, L., Baygents, J. & Saville, D., 1993. The interpretation of dielectric response measurements on colloidal dispersions using the dynamic Stern layer model, *J. Chem. Phys.,* **98,** 4183–4194. https://doi.org/10.1063/1.465108.

Rozycki, A., Ruiz Fonticiella, J.M. & Cuadra, A., 2006. Detection and evaluation of horizontal fractures in earth dams using the self-potential method, *Eng. Geol.,* **82,** 145–153. https://doi.org/10.1016/j.enggeo.2005.09.013.

Schiavon, N., 2007. Kaolinisation of granite in an urban environment, *Environ. Geol.,* **52,** 399–407, https://doi.org/10.1007/s00254-006-0473-0.

Schlumberger, C., 1920. *Etude sur la Prospection Électrique Du Sous-sol,* Gauthier-Villars, Paris. The second edition without modification is available at https://gallica.bnf.fr/ark:/12148/bpt6k64569898.texteImage. English version, translated by Sherwin F. Kelly: "Study of underground electrical prospection". Available at: https://archive.org/details/studyofundergrou00schlrich/page/n37.

Shamsipour, P., Marcotte, D., Chouteau, M., Rivest, M. & Bouchedda, A. 2013. 3D stochastic gravity inversion using nonstationary covariances, *Geophysics,* **78**(2), G15–G24, https://doi.org/10.1190/geo2012-0122.1.

Sheffer, M., 2007. *Forward Modeling and Inversion of Streaming Potential for the Interpretation of Hydraulic Conditions from Self-potential Data: PhD Thesis,* The University of British Columbia.

Shuey, R.T. & Johnson, M., 1973. On the phenomenology of electrical relaxation in rocks, *Geophysics,* **38,** 37–48. https://doi.org/10.1190/1.1440331.

Sill, W.R., 1981. Self-potential modeling from primary flows, DOE Report DOE/ID/12079-42, 52 pp.

Sill, W.R., 1983. Self-potential modeling from primary flows, *Geophysics,* **48,** 76–86. https://doi.org/10.1190/1.1441409.

Soldi, M., Guarracino, L. & Jougnot, D., 2020. An effective excess charge model to describe hysteresis effects on streaming potential, *J. Hydrol.,* **588,** 124949, https://doi.org/10.1016/j.jhydrol.2020.124949.

Soueid Ahmed, A., Jardani, A., Revil, A. & Dupont, J.P.&', 2013. SP2DINV: a 2D forward and inverse code for streaming-potential problems, *Comput. Geosci.,* **59,** 9–16. http://dx.doi.org/10.1016/j.cageo.2013.05.008.

Soueid Ahmed, A., Jardani, A., Revil, A. & Dupont, J.P., 2016. Specific storage and hydraulic conductivity tomography through the joint inversion of hydraulic heads and self-potential data, *Adv. Water Res.,* **89,** 80–90. http://dx.doi.org/10.1016/j.advwatres.2016.01.006.

Soueid Ahmed, A., Revil, A., Abdulsamad, F., Steck, B., Vergniault, C. & Guihard, V., 2020b. Induced polarization as a tool to non-intrusively characterize embankment hydraulic properties, *Eng. Geol.,* **271,** 105604, https://doi.org/10.1016/j.enggeo.2020.105604.

Soueid Ahmed, A., Revil, A., Bolève, A., Steck, B., Vergniault, C., Courivaud, J.R., Jougnot, D. & Abbas, M., 2020a. Determination of the permeability of seepage flow paths in dams from self-potential measurements, *Eng. Geol.,* **268,** 105514, https://doi.org/10.1016/j.enggeo.2020.105514.

Soueid Ahmed, A., Revil, A., Jardani, A. & Chen, R., 2018. Geostatistical inversion of induced polarization data, *Geophysics,* **83**(3), E133–E150. https://doi.org/110.1190/GEO2017-0232.1.

Soueid Ahmed, A., Revil, A., Steck, B., Vergniault, C., Jardani, A. & Vinceslas, G., 2019. Self-potential signals associated with localized leaks in dam embankments and dikes, *Eng. Geol.,* **253,** 229–239. https://doi.org/10.1016/j.enggeo.2019.03.019.

Stern, O., 1924. *Zur theorie der elektrolytischen doppelschicht*, *Z. Elektrochem. Angew. Phys. Chem.,* **30**(21-22), 508–516. https://doi.org/10.1002/bbpc.192400182.

Stoch, L. & Sikora, W. 1976. Transformation of micas in the process of kaolinisation of granites and gneisses, *Clays Clay Miner.,* **24,** 156–162. https://doi.org/10.1346/CCMN.1976.0240402.

Su, Z. *et al.* 2022, Joint interpretation of marine self-potential and transient electromagnetic survey for seafloor massive sulfide (SMS) deposits: application at TAG hydrothermal mound, Mid-Atlantic Ridge, *J. geophys. Res.: Solid Earth,* **127,** e2022JB024496, https://doi.org/10.1029/2022JB024496.

Thanh, L.D., Van Nghia, N., Van Do, P., Du, P.T. & Jougnot, D., 2023, A unified model for the permeability, electrical conductivity and streaming potential coupling coefficient in variably saturated fractured media, *Geophys. Prospect.,* **71**(2), 279–291. https://doi.org/10.1111/1365-2478.13295.

Titov, K., Komarov, V., Tarasov, V. & Levitski, A., 2002. Theoretical and experimental study of time domain-induced polarization in water-saturated sands, *J. appl. Geophys.,* **50,** 417–433. https://doi.org/10.1016/S0926-9851(02)00168-4.

Vinegar, H. & Waxman, M., 1984. Induced polarization of shaly sands, *Geophysics,* **49**(8), 1267–1287. https://doi.org/10.1190/1.1441755.

Waxman, M.H. & Smits, L.J.M., 1968. Electrical conductivities in oil-bearing shaly sands, *Soc. Pet. Eng. J.,* **8**(2), 107–122. https://doi.org/10.2118/1863-A.

Wilson, M.J., 2004. Weathering of the primary rock-forming minerals: processes, products and rates, *Clay Miner.,* **39,** 233–266. https://doi.org/10.1180/0009855043930133.

Woo, I., Fleurisson, J.A. & Park, H.-J., 2006. *Classification of Weathering for Granite and Granite Gneiss in South Korea, IAEG2006 Paper Number 131,* The Geological Society of London.

Xie, J., Cui, Y. & Niu, Q., 2021. Coupled inversion of hydraulic and self-potential data from transient outflow experiments to estimate soil petrophysical properties, *Vadose Zone J.,* **20**, e20157, https://doi.org/10.1002/vzj2.20157.

Yatsu, E., 1988. *The Nature of Weathering*. Sozosha, Tokyo, p 624.

Zhang, K., Chibati, N., Revil, A., Richard, J., Gresse, M., Xue, Y. & Géraud, Y., 2023. Induced polarization of volcanic rocks. 6. Relationships with other petrophysical properties, *Geophys. J. Int.,* **234,** 2376–2394. https://doi.org/10.1093/gji/ggad246.

Zhang, P., Feng, M. & Xu, X., 2024. Double-layer distribution of hydronium and hydroxide ions in the air–water interface, *ACS Phys. Chem. Au,* **4**(4), 336–346. https://doi.org/10.1021/acsphyschemau.3c00076.

THE EXCESS CHARGE DENSITY VERSUS PERMEABILITY

We assume that the porous material is partially saturated with water (wetting fluid) and air (insulating non-wetting fluid). The volume averaging approach is considered below to obtain the macroscopic streaming current density. The effective macroscopic charge densities (in C m^{-3}) dragged by the flow of the two fluid phases is obtained as,

$$\hat{Q}_V(s_w) = \frac{\langle \rho(x)(\dot{u}_w(x) - \dot{u}(x)\rangle}{\langle \dot{u}_w(x) - \dot{u}(x)\rangle}. \tag{A1}$$

$$\langle . \rangle = \frac{1}{V_p}\int_{V_p} (\ .\ ) \mathrm{d}V, \tag{A2}$$

where the brackets denote a pore volume averaging, $\dot{u}(x)$ corresponds to the instantaneous local velocity of the solid phase (usually considered to be negligible except during strong deformation), $\rho(x)$ (in C m^{-3}) denotes the local charge density in the water phase associated with the electrical diffuse layer at the mineral water interface (Delville 1991; Leroy & Revil 2004) and at the air/water interface (Leroy *et al.* 2012; Zhang *et al.* 2024), $\dot{u}_w(x) - \dot{u}(x)$ describes therefore the local instantaneous velocity of the water phase with respect to the solid phase (in m s^{-1}) and is called the filtration velocity, **x** a local position in the pore space of the material, and dV an elementary volume around point $M(x)$. According to this definition of the excess charge density, this is a dynamic properties associated with the texture of the material and not a static property of the electrical double layer (such as the total charge density of the diffuse layer integrated over its thickness, see Leroy & Revil 2004).

The streaming current density used in eq. (9) of the main text is related to the local current density in the water phase and defined as the product of the excess of charge associated with the diffuse layers and the local velocity. This corresponds to the strict definition of the source current density. Therefore, we have,

$$j_S = \theta \langle \rho(\dot{u}_w - \dot{u})\rangle , \tag{A3}$$

$$J_S = \hat{Q}_V(s_w)\theta \langle \dot{u}_w - \dot{u}\rangle , \tag{A4}$$

where q denotes the water content (at saturation $\theta = \theta_S = \phi$ the connected porosity). The filtration displacement (in m) associated with the flow of the water phase is defined as,

$$w = \theta \langle u_w - u\rangle , \tag{A5}$$

and the total current density of electrokinetic nature is given as,

$$j_S = \hat{Q}_V(s_w)\dot{w}. \tag{A6}$$

where $\dot{w}$ is related to the permeability (including the effect of saturation through a relative permeability function) thanks to Darcy's law (which is itself an average of the local momentum conservation equation for the pore water).

We want now to determine the effects of the permeability and saturation upon the dynamic or effective charge density. For the saturation, Revil *et al.* (2007) obtained:

$$\hat{Q}_V(s_w) = \frac{\hat{Q}_V}{s_w}, \tag{A7}$$

where $\hat{Q}_V$ denote the value of the effective charge density at saturation. If we perform a classical streaming potential experiment to determine the so-called streaming potential coupling coefficient, we can determine the dependence of $\hat{Q}_V$ with the permeability. This represents a flow through experiment during which we can also measure the permeability by looking at the flux of water passing through the core sample under a prescribe head gradient. The total current density is defined as

$$j = \sigma_0 E + j_S, \tag{A8}$$

when the total current density is zero (as in a flow through experiment where the sample is between two reservoirs at two different pressures), we obtain,

$$\sigma_0 \nabla\varphi = \hat{Q}_V(s_w)\dot{w}, \tag{A9}$$

and using the Darcy's equation, the streaming potential coupling coefficient is given by (here in V Pa^{-1}),

$$C \equiv \left.\frac{d\varphi}{dp}\right)_{j=0} = -\frac{\hat{Q}_V(s_w)k_r(s_w)k}{\eta_w}, \tag{A10}$$

where p is the fluid pressure (in Pa), $k_r(s_w)$ and k are the relative permeability (dimensionless) and the permeability at saturation (in m^2), and η_w denotes the dynamic viscosity (in Pa·s). Having measured the permeability and the coupling coefficient, we can determine the value of $\hat{Q}_V(s_w)$ and we can report the determined value as a function of the permeability itself. We observe in Fig. 5 that $\hat{Q}_V(s_w)$ is strongly related to the permeability as discussed in the main text. Other models have been recently developed and based for instance on the pore size distribution (Soldi *et al.* 2020: Thanh *et al.* 2023), while classical electrokinetic models are based on the zeta potential (e.g. Leroy & Revil 2004).

INVERSION OF THE SELF-POTENTIAL DATA

The inversion process uses the distribution of the measured (self-) potential values at the ground surface to obtain the distribution of the causative source current density below the ground surface. The problem in itself can be seen as a problem similar to the inverse problem in EEG (see Grech *et al.* 2008) except than in EEG, the source is generally localized and not distributed over a broad support volume. The integral form of the Poisson equation is (e.g. Grech *et al.* 2008; Jardani *et al.* 2008),

$$\varphi(d) = \int_{\Omega} \mathbf{K}(\mathbf{d}, \mathbf{m})\, \mathbf{j_s}(\mathbf{m})\, \mathrm{d}V, \tag{B1}$$

where dV is a volume element around the position of the current density, $\mathbf{K}(\boldsymbol{d}, \boldsymbol{m})$ denotes the kernel function formed by a collection of Green functions connecting the self-potential data at measurement points $\mathbf{d}$ (vector column, $[1,2,3,\ldots,N]^{\mathrm{T}}$) and the sources of current density at a set of source points, $\mathbf{m}$ (vector column, $[1,2,3,\ldots,M]^{\mathrm{T}}$), located in the conducting ground Ω. N denotes the number of self-potential stations while M is the discretized elements composing the ground. $\mathbf{K} = (\mathbf{K}_x, \mathbf{K}_y, \mathbf{K}_z)$ ($\mathbf{K}_x$, $\mathbf{K}_y$, and $\mathbf{K}_z$ are the components of the kernel components on the Cartesian Coordinate System), has three component for each source point $\mathbf{m} = (\mathbf{j}_x, \mathbf{j}_y, \mathbf{j}_z)$. Then, $\mathbf{K}$ is a $N \times 3\ M$ matrix.

In the field work at Lampy, we have $N = 336$ measurements and $M = 11\,902$ discretized elements describing the subsurface volume of interest located below the investigated area Since $M << N$, the problem is underdetermined. The misfit (cost) function, ψ, using Tikhonov regularization can be defined as (e.g. Jardani *et al.* 2008)

$$\Psi = ||\mathrm{W}_d(\mathrm{Km} - \varphi_d)||_2 + \lambda||\mathrm{W}_m(\mathrm{m} - \mathrm{m}_0)||_2, \tag{B2}$$

where λ denotes a regularization parameter, $\mathbf{W}_{\mathrm{d}} = \mathrm{diag}\,\{1/\sigma_1, \ldots, 1/\sigma_N\}$ is a square diagonal weighting $N \times N$ matrix (function of the standard deviation σ_i), $\mathbf{W}_{\mathrm{m}}$ is a $(3M\text{-}1) \times 3\ M$ flatness matrix, $\mathbf{m}$ is the vector of 3 M model parameters (the source current density) and $\mathbf{m}_0$ is a reference model (prior source current density), and $\boldsymbol{\varphi}_{\mathrm{d}}$ is column vector of N elements corresponding to the measured self-potential data. The first term of eq. (A2) corresponds to the data misfit while the second term corresponds to the regularization term

used to make the function convex (so we have $\partial\psi/\partial m = 0$). The matrix $\mathbf{W}_{\mathrm{m}}$ can be determined as a first-order differential operator as (Jardani *et al.* 2008),

$$W_m^1 = \begin{bmatrix} 1 & -1 & 0 & 0 & \cdots & 0 \\ 0 & 1 & -1 & 0 & \cdots & 0 \\ \vdots & & \ddots & \ddots & & \vdots \\ \vdots & & & \ddots & \ddots & \vdots \\ 0 & \cdots & 0 & 1 & -1 & 0 \\ 0 & \cdots & 0 & 0 & 1 & -1 \end{bmatrix} \tag{B3}$$

The solution of the problem corresponding to the minimum of the cost function ψ is given by (Hansen 1998),

$$\mathbf{m}^* = \left[\mathbf{K}^T\left(\mathbf{W}_d^T\mathbf{W}_d\right)\mathbf{K} + \lambda\left(\mathbf{W}_m^T\mathbf{W}_m\right)\right]^{-1} \cdot \left[\left(\mathbf{K}^T\left(\mathbf{W}_d^T\mathbf{W}_d\right)\right)\varphi_d + \lambda\left(\mathbf{W}_m^T\mathbf{W}_m\right)\mathbf{m}_0\right]. \tag{B4}$$

It is important to note that in order to avoid source localization close to the ground surface, the vector $\mathbf{m}$ should be balanced thanks to the sensitivity matrix. In this paper, we used the depth weighting function described and justified by Jardani *et al.* (2008).